

## Latest Edition

Welcome to the September 2014 edition of TCAD News. While 14nm FinFET is close to mass production, the development of 10 and 7nm nodes is well underway. The J-2014.09 release of TCAD Sentaurus includes many new features and enhancements for modeling sub-10nm devices. To name a few, Sentaurus Process now supports multiphase silicidation in 3D and selective epitaxial growth of Ge and SiGe using Lattice Kinetic Monte Carlo (LKMC). In Sentaurus Device, a mole-fraction dependent thin layer mobility model is available for III-V channels. A new interface to a 2D Schrödinger solver can be used to analyze quantization in 2D cross sections of FinFETs and nanowire channels. Updated models in Sentaurus Device Monte Carlo provide an alternative to simulate nanoscale FinFETs with SiGe and III-V channel materials using the Boltzmann transport approach. A new particle-based algorithm in Sentaurus Topography brings significant speed up to the etching and deposition simulation of high aspect ratio holes used in 3D memory devices. In power devices we now include Advanced Calibration settings for GaN and SiC. In BEOL and TSV reliability analysis, Sentaurus Interconnect includes hybrid meshes for more efficient handling of large structures and thermal sub-modeling. In optoelectronics, improved fitting of dispersive media enhance EMW broadband simulations.

Overall, the new release of TCAD Sentaurus has an impressive list of enhancements that extends the modeling coverage for both More Moore and More than Moore devices. I trust that you will find the new enhancements in the J-2014.09 release of TCAD Sentaurus useful for your simulation tasks. As always I welcome your feedback.

With warm regards,

**Terry Ma**  
Vice President of Engineering, TCAD

## Contact TCAD

For further information and inquiries:  
[tcad\\_team@synopsys.com](mailto:tcad_team@synopsys.com)

# TCAD news

## Sentaurus Process

### 3D moving boundary improvements

The new command `Set3DMovingMeshMode` simplifies the setup of moving-boundary problems by setting several parameters automatically. It checks the size of the structure and sets the appropriate parameters for the length scale. It prevents common pitfalls in setting up 3D oxidation and avoids contradicting `MovingMesh` parameters.

Figure 1 shows an example, progressing from an initial 1.5nm native oxide on the left to the final 30nm oxide on the right. The setup for 3D oxidation is:

```
Set3DMovingMeshMode 0.01
diffuse time=10 temp=1050
flowH2=1.0 flowO2=2.0 flowN2=8.0
```

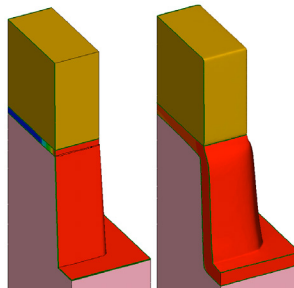


Figure 1: Oxidizing structure at the start and at the end of 3D oxidation.

`MovingMesh` has been improved and tested for 3D silicidation. Figure 2 shows the 3D titanium silicidation in a FinFET structure at 1 second, 10 seconds, and 100 seconds. For clarity, only the outline of titanium is shown. The simulation took 6 hours on 4 threads on a 2933 MHz Intel® Xeon® computer. The final mesh contains about 25,000 vertices and 140,000 tetrahedral elements in 12 regions. The silicide thickness grows from 1nm initially to 8nm in the end.

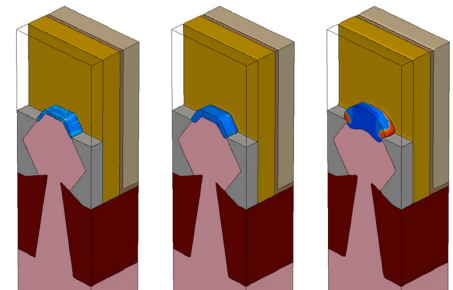


Figure 2: 3D titanium silicidation of a FinFET structure at 1 second, 10 seconds, and 100 seconds.

### Unified handling of alloy materials

Material parameters in random alloys can depend on the mole fraction. In order to capture this effect, Sentaurus Process uses automatic mole fraction dependent parameter interpolation. Once a material has been set up as an alloy of a set of base materials, the mole fraction will automatically be updated and all material parameters which have been interpolation “enabled” will automatically vary throughout alloy regions. For example the alloy  $\text{Si}_{(1-x)}\text{Ge}_x$ , which is given the name `SiliconGermanium`, is composed of base materials `Silicon` and `Germanium`. The atomic concentration of the base materials and the mole fraction, “x”, (named `xMoleFraction`) are stored as fields in the material `SiliconGermanium`.

The following interpolation functions are available: linear, parabolic piecewise linear table, logarithmic and user defined. Parameter interpolation can be turned on and off parameter-wise, module-wise (diffuse, mechanics, MC implant, KMC/LKMC), material-wise, and globally.



### Interface to Sentaurus Visual

A new interactive graphics interface to Sentaurus Visual has been developed for this release. Please see description in “Interactive Interface to Sentaurus Process and Sentaurus Interconnect” on page 22.

### Selective epitaxy of Ge and SiGe with LKMC

Support has been added for homo-epitaxial growth of SiGe and Ge. By default, when the `Epi` option is specified in the `diffuse` command, SiGe will be deposited on exposed SiGe regions or Ge will be deposited on Ge regions. Only one material can grow at a time. Parameters for SiliconGermanium are by default interpolated from their value in the base materials, which in this case are Silicon and Germanium.

### Tighter integration of Kinetic Monte Carlo (KMC) and Lattice Kinetic Monte Carlo (LKMC) with Sentaurus Process

#### Improved support for Like parameter inheritance

The `mater` command can now be used to enable KMC and LKMC parameter inheritance. The `new.like` parameter works for KMC and LKMC the same way as for other modules; all the parameters in the new material will be the same as the “Like” material unless otherwise specified.

#### KMC during continuum silicidation

In addition to the handling of dopants in the moving boundary, the parameters `P_GrowthDeposit` and `E_GrowthDeposit` have been introduced to allow control of dopant transfer across the Silicon/Silicide boundary during silicidation.

#### LKMC support of the reaction command

The reaction command has been enhanced to enable LKMC epitaxy of any material.

### Improved 3 phase segregation model in KMC

Similar to the continuum three-phase segregation, parameters to control the total maximum concentration of trapping sites at an interface have been added: `Factor.Max_Surf` and `Exp.Max_Surf`.

### Control of activation during KMC epitaxy

Parameters `C0_epiMaxActive`, `E_epiMaxActive`, `epiDeposit_Complex` and `epiDeposit_Active`, similar to those used for solid-state epitaxial regrowth (SPER), have been added to control the activation of dopants during epitaxy.

### Hexagonal Crystal Anisotropy for Mechanics

The stress-strain relation in mechanics has been enhanced to improve the accuracy in materials which exhibit hexagonal symmetry. For materials with a hexagonal lattice type such as SiC and  $Al_xGa_{(1-x)}N$ . Sentaurus Process uses five independent elastic stiffness constants: C11, C12, C13, C33, and C44.

### Wavelength Dependence and Reflectance in Laser Anneal

In order to improve accuracy in heat generation during laser annealing, variations in the reflectance and interference of incoming light can now be taken into account. The wavelength and temperature dependent complex refractive indices of materials are set as PDB parameters and the reflectance, transmittance and absorbance for both parallel and perpendicular polarizations are calculated by the transfer matrix method (TMM). TMM assumes that the light is composed of monochromatic plane waves with arbitrary angles of incidence and polarization states. The 2D simulation structure is split into multiple vertical segments. TMM is applied to calculate the heat generation rate in the layer stack structure of each vertical

segment where each layer is assumed to be homogeneous, isotropic, and optically linear. To calculate the heat generation rate with TMM, use:

```
pdbSet Heat Use.TMM 1
pdbSet Heat Wavelength <n>; #nm
```

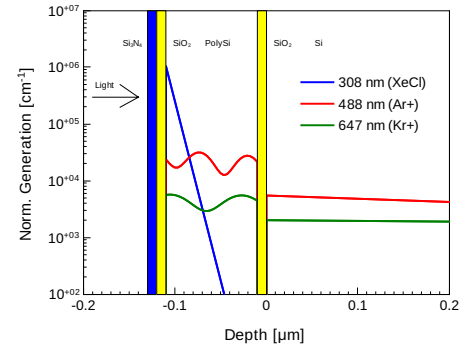


Figure 3: Simulation result for the distribution of normalized heat generation rate for light sources with different wavelengths.

### Re-crystallization of Molten Amorphous Region in Melt Laser Anneal

When an amorphous region melts from exposure to excimer laser illumination, the crystallinity of the region after solidification is determined by the cooling rate. Since the cooling rate is usually small enough to fully crystallize the solidified region, the crystalline phase field is updated by solving the equation:

$$\Delta\alpha = -\alpha \left( 1 - \frac{1}{2} \operatorname{erfc} \left( \ln \left( \frac{\varphi_r}{\varphi + \varepsilon\varphi_r} \right) \right) \right)$$

where  $\alpha$  and  $\varphi$  are the degree of the structural disorder and the melting phase respectively.  $-\Delta\alpha$  is the change of crystallinity per internal time step.  $\varphi_r$  is the parameter to control which melting status begins to lose the crystallinity information. Figures 4a and 4b show the effect of the new model.

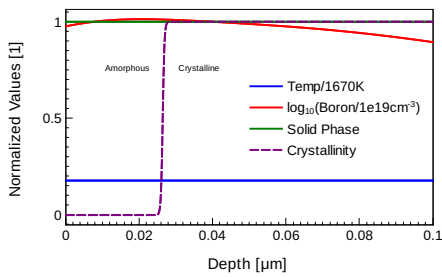


**Figure 4a:** The initial distribution after a Boron implantation with a dose of  $7 \times 10^{13} \text{cm}^{-2}$  and an energy of 5KeV following pre-amorphization Germanium implantation. The entire region is solid and the top  $0.025 \mu\text{m}$  is amorphized.

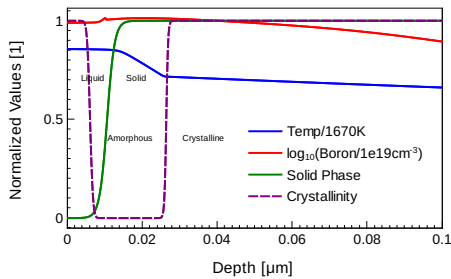


**Figure 4b:** The structure after 130ns exposure, the top  $0.01 \mu\text{m}$  is molten and the crystallinity in the liquid region is changed to zero indicating that the region will be fully recrystallized after solidification.

## Multiphase Nickel Silicidation

In addition to low resistivity ( $12\text{-}20 \mu\Omega\text{-cm}$ ), nickel silicidation has other advantages such as no line width effect, low silicon consumption rate, low film stress, and a low-temperature process. However, nickel silicide has multiple phases which have very different electrical conductivity. Simulating the correct behavior of phase transition during the forming process improves the predictability of subsequent device simulation. The model is invoked by specifying:

```
pdbSet NickelSilicide
Multiphase 1
```

The model takes three irreversible reactions, which are energetically favorable [1], into account as follows:

1.  $2\text{Ni} + \text{Si} \rightarrow \text{Ni}_2\text{Si}$
2.  $\text{Ni}_2\text{Si} + \text{Si} \rightarrow 2\text{NiSi}$
3.  $\text{NiSi} + \text{Si} \rightarrow \text{NiSi}_2$

The  $\text{Ni}_2\text{Si}$  phase is dominant in low temperature nickel silicidation. During the post thermal process after metal strip, the phase transition from  $\text{Ni}_2\text{Si}$  to  $\text{NiSi}$ , and to  $\text{NiSi}_2$  occurs. Since  $\text{NiSi}$  phase has the lowest resistivity, it is advantageous to avoid the high temperature process which drives the phase transition from  $\text{NiSi}$  to  $\text{NiSi}_2$ .

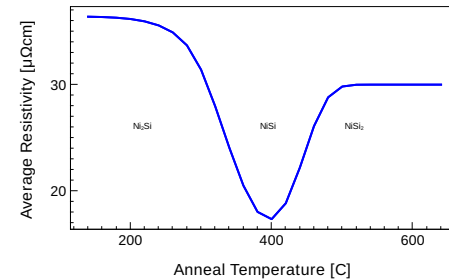


**Figure 5:** Simulation results of the resistivity change of nickel silicide during post anneal process. Although the parameter values are not calibrated yet due to the lack of measured data, the simulation result shows the correct trend of the resistivity change over anneal temperature.

## Unified handling of crystal types and crystal orientation

The J-2014.09 release of Sentaurus Process unifies the syntax and specification of different crystal systems, including specification of crystal type, polytype, crystal orientations, and wafer miscut. Currently, cubic, orthorhombic, and hexagonal systems are supported, but new systems can be easily extended. The following material properties should now be specified in the mater command: crystal system, polytype, lattice constants, and crystal orientations.

The mater command performs some consistency and syntactical checks which were not available with PDB parameters as was used before. In addition, wafer miscut has been re-implemented by using one angle miscut.tilt and one direction miscut.toward. This change makes it easier for process engineers to transfer the wafer specifications to Sentaurus Process parameters.

This improvement is especially important in hexagonal systems such as SiC, since it now allows the specification of SiC crystal orientation and flat orientation as in Silicon. In particular, with this release, the capability of MC implant in SiC is now in parity with Silicon.

## MC implant performance improvement for Extend boundary conditions

In previous releases, when using the Extend boundary condition with the trajectory replication turned off, particles implanted into the extended regions are calculated meticulously just like those implanted into the simulation domain. Because those particles implanted outside simulation domain are largely discarded after the simulation, trajectory replication is now enabled in those extended regions even if trajectory replication is turned off in the simulation domain. This improvement takes advantage of the faster trajectory replication algorithm without sacrificing accuracy in the simulation domain. It is on by default, but can be turned off by using a PDB switch. For typical implant conditions, performance improvements of 10-50% have been observed.

## Performance improvement for 2D analytic implant in 3D mode

The performance of 2D analytic implantation in complex structures using 3D mode has been dramatically improved by simplifying the internal implant interface elements without modifying the simulation mesh. In certain complicated examples, a speed improvement of up to 7x has been observed.



This improvement is enabled by default, but can be turned off by using a PDB switch. In addition, multithreading can be used to further reduce the simulation time for 2D analytic implant in 3D mode: `math numThreadsImp3d=<n>`.

### Improvements to MC implant in SiC

Significant changes have been made to MC implant in SiC:

- ▶ Crystal orientation and/or flat orientation can now be specified in `init` or `mater` command for crystalline SiC.
- ▶ Instead of using two angles (`caxis.tilt` and `caxis.rotation`), wafer miscut is now specified by using one angle `miscut.tilt` and one direction `miscut.toward`.
- ▶ Default value of PDB parameter `d.sim` in SiC has been changed from 0.5 to 0.25.

With these improvements, the capability of MC implant in SiC is now in parity with Silicon. However, due to these changes, slightly different results in MC implant may be observed in this release relative to previous releases. A backward compatibility mode is available.

### Loading 3D data into 2D structures

Loading data from a 3D TDR file to a 2D simulation is now available through the `load` command. Field data from the 3D structure is read from the `z=0` slice. However, the `load` command allows the user to transform the 3D structure before reading the data, thereby allowing the loading of data on any cross sections. For example, the following command loads the data from the 3D structure at `z = 0.5`:

```
load tdr=source3d transform =
{ 1 0 0 0 1 0 0 0 1 0. 0. -0.5 }
```

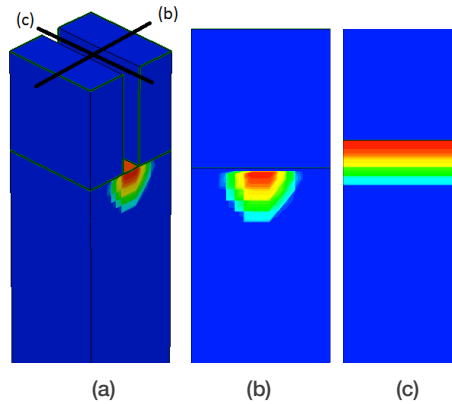


Figure 6: Data interpolated from different cross sections of a 3D structure into a 2D simulation. (a) 3D structure and data. (b) 2D structure with data loaded from (a) as indicated by the (b) cross section. (c) 2D structure with data loaded from (a) as indicated by the (c) cross section.

### Saving 2D structures from 3D

It is now possible to save a 2D structure from a 3D simulation. By specifying an axis-aligned slice using the `x`, `y`, or `z` parameters of the `struct` command, a 2D TDR file is created. This file can be used to start a new 2D process simulation or as input for device simulation. For example, the following command saves a 2D slice of the 3D structure at `x = 0.2` to a 2D TDR file,

```
struct tdr = filename x=0.2
```

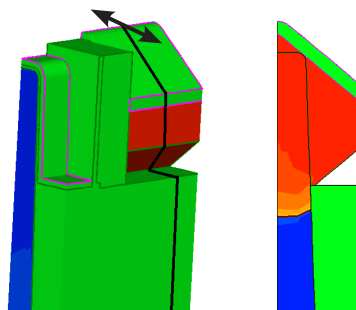


Figure 7: Save a 2D structure from a 3D simulation. (a) Current 3D structure. (b) Structure in 2D TDR file saves at cross section indicated by a black line in (a).

### Crystallographic doping

Sentaurus Process can now account for graded doping as a function of time for crystallographic deposition. Previously, graded doping was only applied isotropically, which may not be suitable for crystallographic deposition. A new parameter `times` has been added to the doping command to give proper anisotropic contours when the doping specification is used in a crystallographic deposition. For example:

```
doping name=strainGe
field=Germanium times= {0.0
0.015} values= {1e22 2e22}
deposit type=crystal doping=
{strainGe} material=Silicon
time = 0.015
crystal.rate = { <100>=1.0
<110>=0.1 <111>=0.9 }
selective.materials=Silicon
```

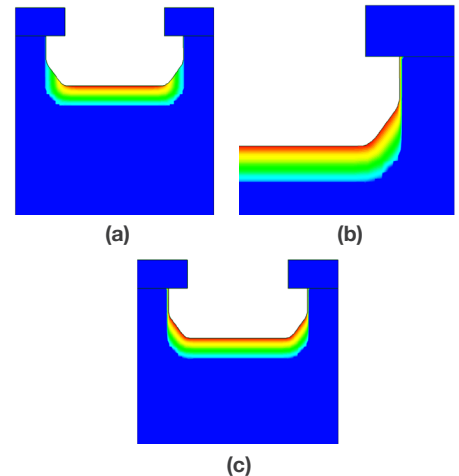


Figure 8: Doping profiles. (a) Anisotropic contours as a result of the `times` parameter of the doping command, (b) zoom-in (c) Isotropic doping contour - notice the contour lines are equidistant from the starting (blue) surface.

## Mesh suppression in 3D etch and deposit

A new option is available for 3D etching and deposition which can be used to reduce calls to mesh generation and thereby reduce simulation time. In 3D simulations, meshing can be suppressed using the `suppress_remesh` parameter of the `deposit` and `etch` commands. For a given uninterrupted sequence of etch and deposit steps, forgoing mechanics and mesh updates until after the last step is often a good tradeoff between simulation time and accuracy. Performance improvement depends on the time required to create a mesh in the structure being simulated, and therefore the chosen mesh density, but significant gains have been observed for typical situations.

## Improved trapezoidal etch boundary quality

The quality of the shapes produced by trapezoidal etching was improved. Now the shapes are more regular and smooth and will not present the noise which used to cause problems in subsequent etching or deposition steps.

## Boolean mask operation enhancements

The scale and rotate operations in the mask command now accept a centering parameter. Before the mask is scaled or rotated, it is shifted to a centering coordinate where the regular operation takes place. After the operation is done, the mask is shifted back to its original location.

## Sentaurus Interconnect

### Mixed Mesh for Mechanics

In this release, we have added the capability to carry out mechanics simulations using hybrid meshes as compared to triangular (2D) and tetrahedral (3D) meshes. The hybrid mesh includes triangular and rectangular elements in 2D and tetrahedral, prism,

pyramid, and brick elements in 3D. The motivation for using a hybrid mesh is to provide better mesh quality and solutions, better accuracy, and avoid known issues such as locking. If linear triangular and tetrahedral elements are used for bending problems, shear locking occurs, that is, the associated shape functions lead to spurious shear strain. In contrast, hybrid meshes are much better suited for bending type problems. The use of brick elements also greatly reduces the element count in the mesh, thus enabling larger simulations such as wafer scale simulations.

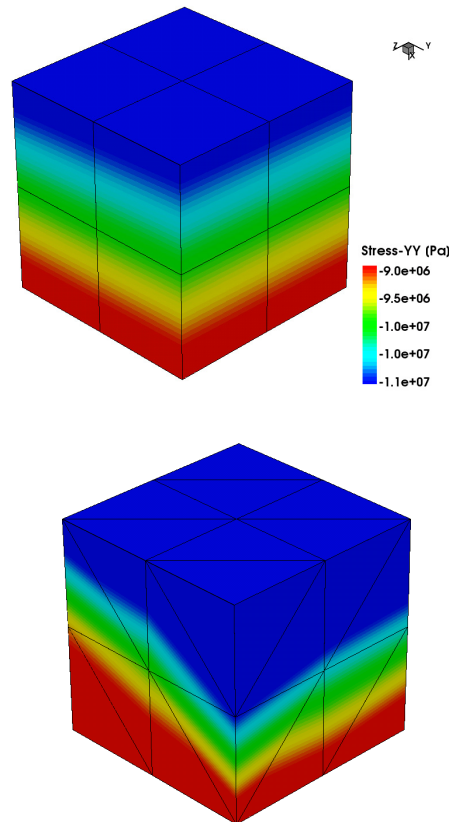


Figure 9: Stress field computed on brick (left) and tetrahedral (right) elements.

Figure 9 illustrates the decreased dependency of brick elements on mesh symmetry, as compared to tetrahedral elements, providing a more accurate solution.

Figure 10 shows the solution obtained from a hybrid brick mesh for a 4-point bending problem. It can be clearly seen that the brick elements do not suffer from locking and, produce accurate symmetrical results.

The material models available with mixed meshes are elastic, viscoelastic, viscoplastic, incremental/deformation plasticity, creep, swelling and anisotropic model. Submodeling capability is also available with hybrid meshes.

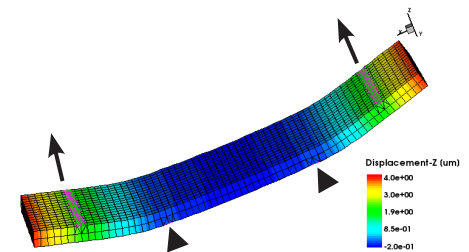
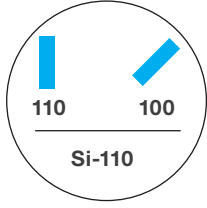


Figure 10: Four-point bending simulations using brick elements. The back arrows indicate the applied forces and the triangles indicate the clamping boundary conditions.

## FinFET mobility

Sentaurus Interconnect has the capability to calculate stress-induced mobility enhancements as a post-processing parameter following a mechanics solution. For planar devices, the mobility model uses piezoresistance coefficients along the crystal axes to calculate the enhancement. However, when modeling non-planar devices, such as FinFETs, the planar assumption needs to be modified to account for the third dimension. The improved FinFET mobility model calculates the enhancement for a (110) or a (100) fin orientation.



The (110) and (100) fin orientation differ in their angle relative to the wafer flat. The carrier type can be an electron or a hole.

Figure 11 shows the mobility calculated in a p-FinFET device as a result the stress. The corresponding stress field is also shown.

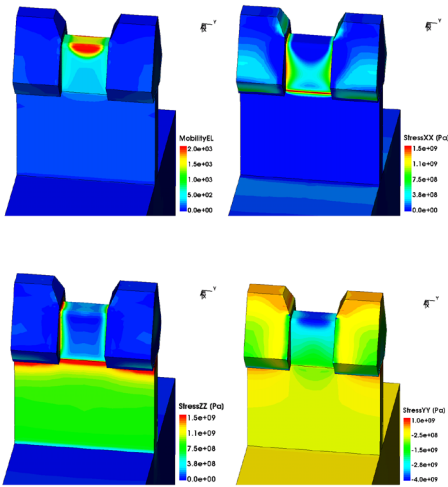


Figure 11: Top left: Stress-dependent mobility calculated for a p-FinFET. Other panels: Components of the corresponding stress field.

### Incremental Plasticity Model with Nonlinear Hardening

The incremental plasticity model in Sentaurus Interconnect has been enhanced to include material nonlinear hardening. For isotropic hardening, the nonlinear behavior is described by an exponential expression [2]:

$$\sigma_y(\alpha, T) = \sigma_{y0}(T) + R_{iso} [1 - \exp(-b_{iso} \alpha)]$$

where  $\sigma_{y0}(T)$  is the yield stress at temperature  $T$  and zero accumulated equivalent plastic strain ( $\alpha=0$ ),  $R_{iso}$  is the maximum increase in yield stress, and  $b_{iso}$  is a model parameter.

For Kinematic hardening, the nonlinear behavior is modeled using Armstrong-Frederick model [3] for evolution of back stress

$$\dot{q}_{ij} = \left( H_k n_{ij} - \sqrt{\frac{2}{3}} H_{NLk} q_{ij} \right) \dot{\alpha}$$

where  $q_{ij}$  is back stress,

$$n_{ij} = \left( \frac{S_{ij}}{\sqrt{S_{ij} S_{ij}}} \right)$$

$S_{ij}$  is deviatoric stress,  $H_{kin}$  is the linear kinematic hardening modulus, and  $H_{NLkin}$  is the material parameter for nonlinear kinematic hardening.

Additionally, a linear model for variation of yield stress with temperature is provided as:

$$\sigma_{y0}(T) = \sigma_0 \left( 1 - \frac{T}{T_0} \right)$$

where  $\sigma_0$  is the yield stress at zero absolute temperature and  $T_0$  is a reference absolute temperature.

### Mukherjee-Bird-Dorn Creep Model

A new creep model is added to take into account the effect of grain size on creep behavior [4]. The new creep model can be expressed as:

$$\dot{\epsilon}^{cr} = \frac{A G b}{k T} D_0 \exp(-Q/RT) \left( \frac{b}{d} \right)^p \left( \frac{\sigma}{G} \right)^n$$

where  $A$  is a dimensionless constant,  $D_0$  is a frequency factor for diffusion,  $G$  is the material shear modulus,  $k$  is the Boltzmann constant,  $Q$  is the activation energy,  $R$  is the universal gas constant,  $T$  is the absolute temperature (Kelvin),  $b$  is the magnitude of the Burgers vector,  $D$  is the grain size (diameter),  $p$  and  $n$  are exponents. The model can be used with or without the Grain Growth model. In the absence of the Grain Growth model, the grain size must be specified with `GSize` field.

To demonstrate the effect of nonlinear hardening on plastic behavior a test problem with a thin copper film deposited

on silicon substrate under cycling thermal loading is simulated with the Bailey-Norton creep model for the first thermal cycle and incremental plasticity with temperature dependent (exponential) yield stress, linear isotropic hardening and nonlinear kinematic hardening for subsequent cycles. The results for variation of copper biaxial stress with temperature are shown in Figure 12.

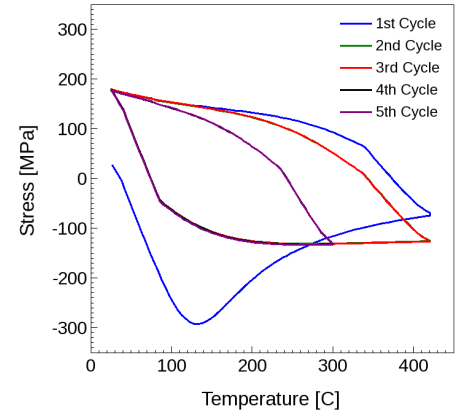
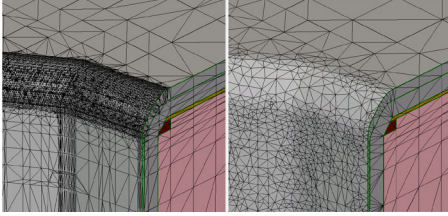


Figure 12: Stress vs. temperature results for test problem with Bialely-Norton creep in 1st cycle and nonlinear kinematic hardening in 2nd through 5th cycles.

### Non-axis aligned mesh for curved surfaces

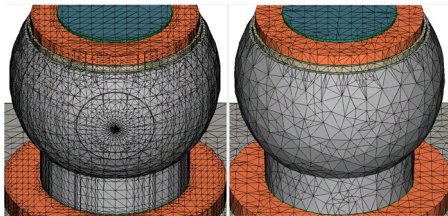
The new command `SetMechanicsMeshMode` sets the meshing parameters for 3D mechanics simulation in large structures such as chip-package interfaces. After this command is executed, subsequent mesh generation commands (for example, `grid remesh`) will generate meshes that are suitable for stress analysis. Triangles on curved surfaces will be more equilateral, and the ones on planar surfaces will continue to be axis-aligned.

Figure 13 shows the default axis-aligned mesh on the left and the new mesh from `SetMechanicsMeshMode` on the right. The latter has better mesh quality, improves convergence and reduces artificial stress hot spots in mechanics simulations.



**Figure 13: Default axis-aligned mesh on left and the new mesh from SetMechanicsMeshMode on right.**

Figure 14 shows meshes for plasticity simulation of solder bumps with the default axis-aligned mesh on the left and the new mesh from SetMechanicsMeshMode on the right. The new mesh enables the plasticity simulation to converge significantly faster and improve simulation results.



**Figure 14: Meshes of solder bumps. Default axis-aligned mesh on left. New mesh on right.**

### Stress dependent grain growth model

The Sentaurus Interconnect J-2014.09 release of Sentaurus Interconnect also includes enhancements to the grain growth model. The growth of the grains size  $L_g$  is given by [5]:

$$\frac{\partial L_g}{\partial t} = GIS \frac{D_{lg} E_{gb}}{L_g kT}$$

where  $E_{gb}$  is the surface energy per atom associated with the grain boundary,  $D_{lg}$  is the effective self-diffusivity in the vicinity of a grain boundary and GIS is the stress dependent grain growth factor. Grain growth means grain boundary elimination, which can lead to the evolution of stress. Using the model of spherical grains, the polycrystalline metal is dilated relative to the previous state with smaller grains [6] and GIS is given by:

$$GIS = \left( 1 - \frac{2}{3} \frac{w^2}{E_{gb}} \left( \frac{E}{1-\nu} \right) \left( \frac{1}{L_{g0}} - \frac{1}{L_g} \right) \right)$$

where  $w$  is the width of a grain boundary,  $E$  is the Young's modulus,  $\nu$  is the Poisson ratio and  $L_{g0}$  is the initial grain size. During grain growth, the elastic strain energy increases along with the stresses and strains in the structure which may stop grain growth. If the initial grain size  $L_{g0}$  is greater than the critical value, the grains will grow freely until a single crystal state is reached. The strain energy will not be enough to stop the grain growth. However, if the initial grain size is less than the critical value, the initial grain size must be sufficiently small to be able to stop grain growth [7].

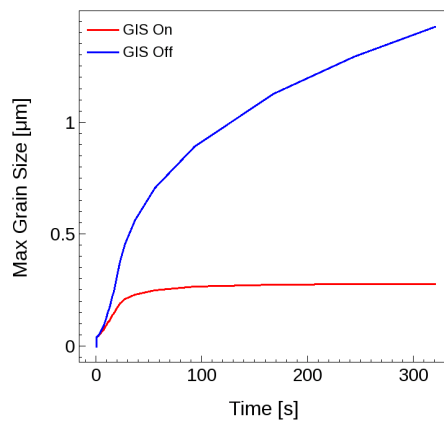


**Figure 15: Maximum grain size vs. time with and without GIS.**

Figure 15 shows the comparison of grain growth with and without stress dependency.

### Thermal Submodeling

Electro-thermal simulations with Sentaurus Interconnect can be performed for various scales of structures. The simulation structures can change from large structures such as chip-packages to small, detailed structures such as single devices on the chip. In most cases it is desirable to include thermal simulation results of larger structures as boundary condition for the smaller structures in order to speed up their simulations and get consistent results. This

is referred as thermal submodeling and works similarly to mechanical submodeling. In Sentaurus Interconnect J-2014.09 release enhancements have been made to thermal modeling capabilities to allow thermal submodeling.

New command parameter `thermal.global.model` is added to the mode command. If the global model is provided with the new parameter, the thermal simulation result (`Temperature`), from the global model is used as boundary condition during the next thermal analysis. If the global model is not provided, the sub modeling simulation is performed using the temperature profile at the next thermal analysis step as boundary condition.

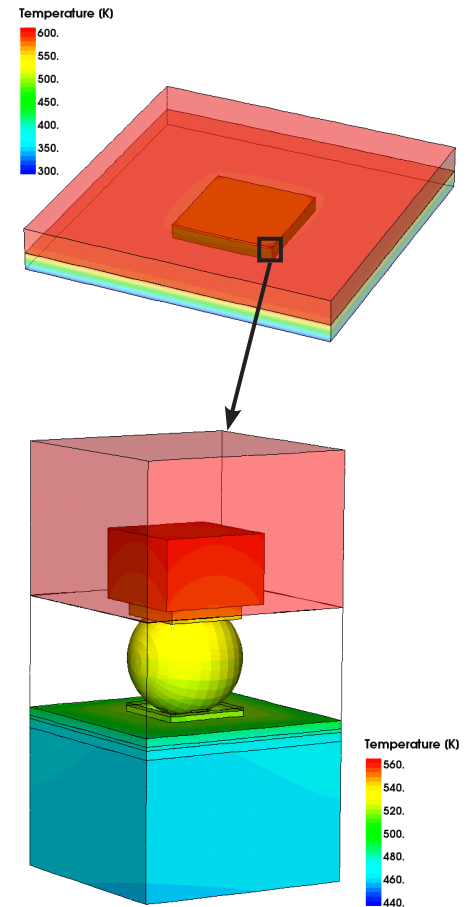


**Figure 16: Temperature profiles in global model including the entire package and the submodel containing only a single solder bump at the corner of the die.**



Figure 16 shows the temperature profiles in both global structure and submodel structure. The temperature profile from the global model is used as boundary condition for the submodel structure. The submodel results also include joule heating within the solder bump due to current flow.

## Sentaurus Topography 3D

### Reaction Modeling with the Particle Monte Carlo Method

A new class of models, namely, *reaction models*, is now available as a product option in Sentaurus Topography 3D to describe the physical and chemical effects that occur on a wafer surface due to interaction with species present in the reactor (typically provided by a plasma source). Effects such as adsorption, deposition, re-emission, reflection, and sputtering can be included in reaction models using a syntax that is similar to that used for chemical reactions [19]. Users can define their own reaction models by combining the available effects in an arbitrary way.

Each reaction defines the interaction of a single gas-phase species with one surface species, along with the products that may result from this interaction. Reaction products can be emitted from the surface and eventually interact with other parts of the wafer surface, or they can be defined as being volatile, meaning that they have no effect in the simulation.

Reaction models are simulated using the Particle Monte Carlo (PMC) method, which is an efficient stochastic particle-based simulation method which often outperforms the level set-based engine in execution speed.

In the following, the results of PMC simulations for two applications are presented to illustrate capabilities and performance of the new reaction models of Sentaurus Topography 3D. The modeling and simulation of an SF<sub>6</sub>/O<sub>2</sub> etching process for high-aspect-ratio (HAR) holes as well as layout-based etching and fill of a trench are presented.

### Etching of High-Aspect-Ratio Holes Using SF<sub>6</sub>/O<sub>2</sub> Plasma

SF<sub>6</sub>/O<sub>2</sub> plasma-based processes are used for etching HAR holes in silicon structures. In an SF<sub>6</sub>/O<sub>2</sub> process, SF<sub>6</sub> molecules dissociate in the reactor and provide ions (SF<sub>3</sub><sup>+</sup>) as well as highly reactive fluorine (F) atoms. In particular, fluorine atoms are adsorbed on silicon and produce SiF<sub>x</sub> molecules, which can eventually become volatile due to a chemical etching reaction, resulting in silicon etching. At the same time, SiF<sub>x</sub> molecules are etched by SF<sub>3</sub><sup>+</sup> ion bombardment. To achieve anisotropic etching, O<sub>2</sub> gas is also fed to the reactor. In fact, atomic oxygen adsorbs on silicon and slows down chemical etching by fluorine, but it is desorbed by SF<sub>3</sub><sup>+</sup> ions. Since SF<sub>3</sub><sup>+</sup> ion trajectories are almost vertical, oxygen atoms that adsorbed on the bottom of the hole are desorbed, but those that adsorbed on the sidewalls are not. Therefore, the sidewalls are etched significantly less than the bottom, which results in anisotropic etching. In addition, SF<sub>3</sub><sup>+</sup> ions etch the photoresist mask and can be reflected by the vertical sidewalls of the hole as well.

A Sentaurus Topography 3D reaction model for this process can be set up by encoding each relevant mechanism into a reaction, as shown in the following code:

```
define_model name=m
description="SF6/O2 etch
process"
add_source_species model=m
name=F
add_source_species model=m
name=SF3+
add_source_species model=m
name=O
add_reaction model=m name=R1
expression="F<g> + Silicon<s>
= SiFx<s>"
add_reaction model=m name=R2
expression="F<g> + SiFx<s> =
SiFy<v>"
add_reaction model=m name=R3
expression="SF3+<g> + SiFx<s>
= SF3* <v> + SiFx<v>"
add_reaction model=m
name=R4 expression="SF3+<g>
+ Silicon<s> = SF3+<r> +
```

```
Silicon<s>"
add_reaction model=m name=R5
expression="O<g> + Silicon<s>
= SiO<s>"
add_reaction model=m name=R6
expression="SF3+<g> + SiO<s> =
Silicon<s> + O<v> + SF3* <v>"
add_reaction model=m
name=R7 expression="SF3+<g>
+ Photoresist<s> =
Photoresist<v>"
add_reaction model=m name=R8
expression="SF3+<g> +
Photoresist<s> = SF3+<r> +
Photoresist<s>"
finalize_model model=m
```

The effects modeled by each reaction are summarized in Table 1.

Reaction	Modeled effect
R1	Fluorine adsorption on silicon
R2	Chemical etching of SiF <sub>x</sub>
R3	Etching of SiF <sub>x</sub> by SF <sub>3</sub> <sup>+</sup> ion bombardment
R4	Reflection of SF <sub>3</sub> <sup>+</sup> ions by silicon
R5	Oxygen adsorption on silicon
R6	Oxygen desorption by SF <sub>3</sub> <sup>+</sup> ion bombardment
R7	Photoresist etching by SF <sub>3</sub> <sup>+</sup> ion bombardment
R8	Reflection of SF <sub>3</sub> <sup>+</sup> ions by photoresist

Table 1: Effects modeled by each model reaction.

As can be seen, reactions are defined using a syntax that is very similar to the syntax used for chemical reactions. Also, ion reflection is included in the model by reactions R4 and R8 that use the special species term modifier <r> [19].

In a reaction model, an execution probability is associated with each reaction. Reaction probabilities dependent on the angle between the direction of the incoming particles and the normal to the surface at the reaction location can be used to properly model effects such as ion reflection. For brevity, the reaction probabilities used in the discussed model are not reported here.



To use the above-defined reaction model, the angular distributions of each source species (namely, F, O, and  $SF_3^+$ ) have to be defined as well as their absolute fluxes entering the reactor. Since F and O are electrically neutral, their angular distributions will be modeled as isotropic; whereas, the angular distribution of  $SF_3^+$  ions will be focused around the vertical direction of the reactor (an exponent [8] of 5000 is used). In addition, unlike the level set-based models of Sentaurus Topography 3D, reaction models require the specification of the absolute fluxes of the source species.

The setup reaction model has been used to simulate an  $SF_6/O_2$  plasma-based process to etch an HAR hole in a silicon structure covered by a photoresist mask with a circular opening. The mask height is 30  $\mu m$  and the mask opening diameter is 0.1  $\mu m$ . The mesh size used for the simulation is 5 nm along each coordinate direction.

Figure 17 shows the initial structure as well as the structures obtained at the end of the simulated process for different values of the oxygen flux. In particular, for a fixed fluorine flux, the oxygen flux is varied and, namely, the oxygen-to-fluorine flux ratios of 0.1, 0.5, and 1 are considered.

As can be observed, the varying fraction of oxygen gas fed to the reactor affects the etch depth as well as the hole profile. The aspect ratio of the obtained trenches is approximately 31, 37, and 41, respectively. Moreover, as expected from the process description, the amount of lateral etching decreases as the oxygen flux increases.

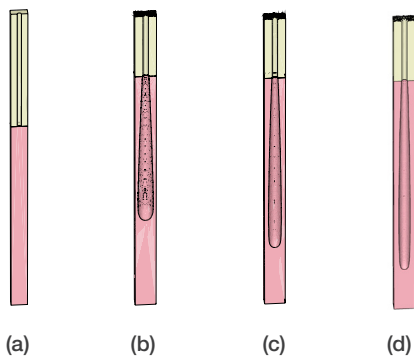


Figure 17: Initial structure (a), final structure with an oxygen-to-fluorine flux ratio of 0.1 (b), 0.5 (c), and 1 (d).

Sentaurus Topography 3D allows you also to study how the surface coverage of the involved chemical species evolves during the process. The surface coverage of a species is the fraction of the surface occupied by that species. The surface coverage of any surface species can be visualized at intermediate times to obtain insights into the process chemistry. In Figure 18, the surface coverage of SiO is shown at intermediate times during the simulated process having an oxygen-to-fluorine-flux ratio of 0.5. As can be seen, the SiO surface coverage is about 1 on the sidewalls and very low on the bottom of the hole. This shows that oxygen protects the sidewalls from fluorine etching, but it is desorbed from the bottom of the hole by the  $SF_3^+$  ions, thereby increasing the etching rate and anisotropy.

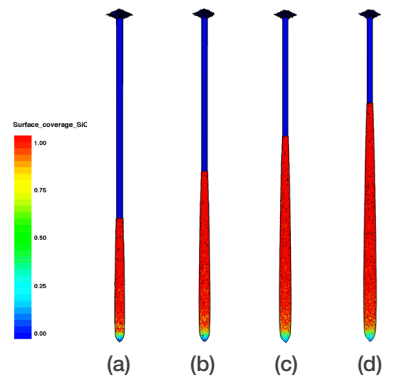


Figure 18: SiO surface coverage during the process having an oxygen-to-fluorine flux ratio of 0.5: at 25% of the process time (a), at 50% of the process time (b), at 75% of the process time (c), at the end of the process (d).

### Trench Etching and Filling Using a Layout

In this section, a three-step flow is simulated. In the first step, a trench is etched in a silicon structure using a mask. The initial structure is shown in Figure 19.

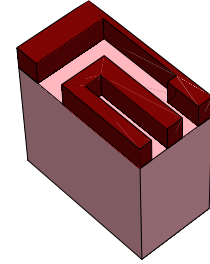


Figure 19: Initial structure with the hard mask for the three-step process.

The etched trench is then filled with TEOS in the second step. Finally, poly-Si is deposited on TEOS. The first two steps are simulated using reaction models; whereas, the last deposition step uses the built-in level set-based simple model.

The model used in the first step is an ion-enhanced etching model assisted by simultaneous polymer deposition. It uses three fluxes: a fluorine (F) flux that adsorbs on silicon, a flux of ions ( $SF_3^+$ ) that etches the adsorbate, and a neutral flux (Pre) that forms a protective layer (Plmr) inhibiting fluorine adsorption. The reactions that describe the aforementioned mechanisms are included in the reaction model defined here:

```
define_model name=m1
description="Ion-enhanced
reaction model with polymer
deposition"
add_source_species model=m1
name=F
add_source_species model=m1
name=Pre
add_source_species model=m1
name=SF3+
add_reaction
model=m1 name=ads_F
expression="Silicon<s> + F<g>
= SiF<s>"
add_reaction model=m1
name=polymer_Si
expression="Silicon<s>
+ Pre<g> = Plmr<s> +
Silicon<b>"
add_reaction model=m1
name=polymer_PR
expression="Oxide<s> + Pre<g>
= Plmr<s> + Oxide<b>"
add_reaction model=m1
name=polymer_SiF
expression="SiF<s> + Pre<g> =
```



```
Plmr<s> + SiF<b>"
add_reaction model=m1
name=ion_etch
expression="SiF<s> + SF3<g> =
SiF<v>"
add_reaction model=m1
name=ion_etch_Plmr
expression="Plmr<s> + SF3<g>
= Plmr<v>"
finalize_model model=m1
```

The distributions of the fluxes are specified for each of the defined species using the `define_species_distribution` command [19]:

```
define_species_distribution
exponent=1000 name=species_
dist species=SF3+ flux=4.0e-4
define_species_distribution
exponent=1 name=species_dist
species=F flux=7.0e-4
define_species_distribution
exponent=1 name=species_dist
species=Pre flux=1.0e-4
```

The `exponent` parameter determines the directionality of the flux [19].

The deposition model is simple: A precursor of TEOS (Pre) is deposited isotropically on all the exposed materials. It is necessary to define a deposition reaction for each of the materials:

```
define_model name=m2
description="Isotropic
deposition reaction model"
add_source_species model=m2
name=Pre
add_reaction model=m2
name=TEOS_Si
expression="Silicon<s>
+ Pre<g> = TEOS<s> +
Silicon<b>"
add_reaction model=m2
name=TEOS_Oxide
expression="Oxide<s> + Pre<g>
= TEOS<s> + Oxide<b>"
add_reaction model=m2
name=TEOS_SiF
expression="SiF<s> + Pre<g> =
TEOS<s> + SiF<b>"
add_reaction model=m2
name=TEOS_TEOS
expression="TEOS<s> + Pre<g>
= TEOS<s> + TEOS<b>"
add_reaction model=m2
name=TEOS_Plmr
```

```
expression="Plmr<s> + Pre<g>
= TEOS<s> + Plmr<b>"
finalize_model model=m2
```

The results from the etching and deposition steps show that there is, as expected, a modulation of the trench width and depth as well as of the trench filling as a function of the size and aspect ratio of the features (Figure 20 (a) and (b)).

The last poly-Si layer (Figure 20 (c)) has been deposited using the level-set model `simple` in order to demonstrate that it is possible to use both methods in the same process flow. This is important in cases where users have an existing library of calibrated level set-based process models and want to use them along with reaction models.

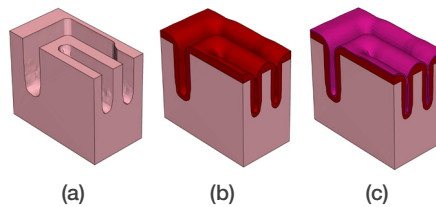


**Figure 20: Final structure obtained after the etching step and mask strip (a), after the TEOS deposition (b), and after the poly-Si deposition (c).**

The calibration of the etching and deposition steps is a critical stage in topography simulations. The new PMC-based reaction models enable a significantly faster calibration of the process steps. In this example, the etching process has been the most time-consuming step for calibration. For comparison, this etching step was simulated also using a level set-based model (`etchdepo2`) that captures the same key effects. The elapsed simulation time for the PMC-based model (single thread) was about 10 times shorter than for the level set-based one (12 threads) for the same grid resolution.

The dramatically reduced simulation time allows users to better fine-tune their layouts in the same timeframe as shown in the present example.

## Sentaurus Device

### Interface to 2D Schrödinger Solver

About 15-20 years ago, microelectronic devices became so small that quantization became important. The state-of-the-art devices of the time were planar MOSFETs. For downscaling, the channel doping was progressively increased, which in turn reduced inversion layer thickness. When the inversion layer is just a few nanometers thick, the quantum-mechanical nature of electrons becomes apparent: The inversion layer charge is smaller than predicted classically, and the peak of the charge density is moved from the channel/insulator interface into the channel. These microscopic changes translate to an increased threshold voltage and a reduced gate capacitance.

At the same time, in quantum-mechanical terms, the channels remained long and wide. Therefore, it was possible to adequately describe quantization with 1D models. Sentaurus Device offers a selection of such models. A 1D Schrödinger solver provides a precise description of physics. As the 1D Schrödinger equation is time consuming to solve, simpler alternatives are available as well. The simpler models might need calibration, which can be achieved by matching the results of the 1D Schrödinger equation.

With the advent of FinFETs, the situation became more complicated. As long as the fin is either wide or much higher than wide 1D quantization models still work. However, as the crystal orientation at the channel/insulator becomes position-dependent, the 1D models have to use calibration parameters that depend on the crystal orientation of nearby interface points. Sentaurus Device was consequently enhanced to automatically pick the correct parameter set at each point in the device.

However, for the purpose of calibration and validation, a reliable reference that describes the 2D channel cross section in a truly 2D manner was missing. Furthermore, nanowires or similar devices are on the



doorstep. Their channel cross section is of quantum scale in both directions, thus a 2D confinement treatment is inevitable. While the Density Gradient (DG) model handles 2D confinement, calibration and validation becomes even more important.

For this reason, in version J-2014.09, Sentaurus Device supports an interface to the 2D Schrödinger solver in Sentaurus Band Structure. To use this interface, users create 2D cross sections ("slices") of the channel of the 3D device as illustrated in Figure 21. During a simulation, Sentaurus Device connects to Sentaurus Band Structure to request a solution of the 2D Schrödinger equation on each of the slices. The resulting 2D quantum-mechanical carrier densities are transferred back to Sentaurus Device and translated into an effective band-edge shift ("quantum potential"). By interpolating this quantum potential in between the 2D slices, Sentaurus Device constructs a 3D quantum-corrected density distribution that enters device simulation in the same way as for "traditional" quantum models like MLDA or DG.

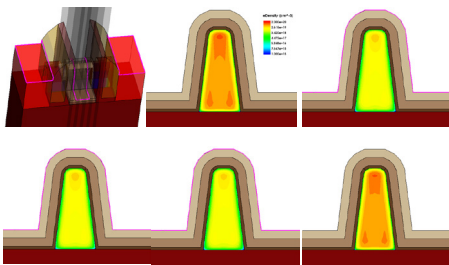


**Figure 21: A set of slices through the channel areas of a FinFET is defined (top left panel). For the Sentaurus Device calls the 2D Schrödinger solver to obtain the quantum-mechanical carrier densities which are then transferred back to Sentaurus Device.**

Sentaurus Device ensures that the 2D Schrödinger equation is solved self-consistently with the Poisson and transport equations. This implies that for each Newton step, the 2D Schrödinger equation is solved once for each of the slices. To keep the computational burden low, it is important to keep the number of slices low. As users

create the slices themselves, they have full control over this. In many cases, using two slices, one at each end of the channel, is sufficiently accurate. If the cross section varies strongly along the channel, more slices can be used.

The 2D Schrödinger solver is parameterized by a Sentaurus Band Structure command file. By keeping control over the 2D Schrödinger solver with Sentaurus Band Structure, all features available there (for example, effective mass, k-p Hamiltonians) become available to Sentaurus Device, and the usage remains consistent with the stand-alone behavior of Sentaurus Band Structure.

## Impedance Field Method

### Local metal conductivity variability

Depending on the growth conditions, metal vias and lines may consist of grains with different sizes and different conductivities. This results in a distribution of the overall effective resistance. The J-2014.09 release of Sentaurus Device now allows the investigation of such variability effects using the impedance field method (IFM), for both the noise-like and the statistical approaches. To use this feature, the metal via or line has to be included in the structure as an actual region and not just as a contact. Users can then assign an average grain size, and probabilities for specified conductivity values per grain. Alternatively, users can assign a standard deviation of the local conductivity as well as a spatial correlation length.

From the solution for the device with a homogenous conductivity Sentaurus Device then computes the current responses due to the local conductivity variability using a linear response approach.

This method may also be used to evaluate the effect of random local contact resistance variability. In this case users define a small effective metal layer between the electrical contact and the semiconductor region, assign an effective contact conductivity to this metal layer, and also define the variability for this quantity.

### Resistance variability of a lumped resistor

The J-2014.09 release also supports the calculation of the effects of variability of a lumped resistor attached to a device terminal as a pure post-processing step. This post-processing is done in Sentaurus Visual in a manner similar to the post-processing of the Sentaurus Device IFM data, with the exception that users specify the lumped resistance variability parameters directly in Sentaurus Visual and not in Sentaurus Device.

Figure 22 compares the gate voltage standard deviations due to local conductivity variability of the metal leads for a FinFET structure with the IFM conductivity variability to an effective modeling of the same effect as resistance variability of an external lumped resistor, again based on IFM. While the latter does not capture the local current-spreading effects it can still reproduce the general trends after proper calibration.

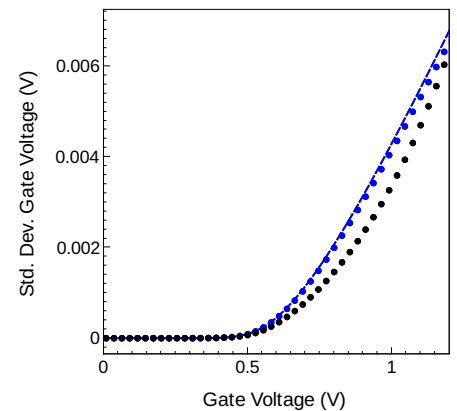


**Figure 22: Standard deviations of the gate voltage as function of gate voltage due to local conductivity variability of the metal leads for a FinFET structure computed with the IFM conductivity variability (blue curves) and an effective modeling of the same effect as resistance variability of an external lumped resistor, again based on IFM (black curves). The dotted lines show results from statistical IFM for both the local conductivity variability and the lumped resistor variability, the dashed line for noise-like IFM for local conductivity variability.**

### Local dielectric constant variability

In a manner similar to local metal conductivity variability you now can also investigate the effect of local variability of the dielectric constant in an insulator using the impedance field method. Such variability again may stem from growth conditions, but this feature can also be used to mimic variability of the thickness of, for example, a thin gate oxide layer. This can be seen as an easier-to-use alternative to layer thickness variability simulations with geometric IFM.

Figure 23 compares the gate voltage standard deviations due to local dielectric constant variability of the gate oxide for a FinFET structure to geometric thickness variability of the gate oxide layer. The figure shows that both variability sources result in quite similar responses.

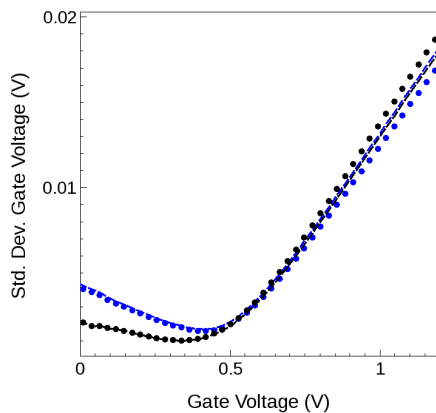


Figure 23: Standard deviations of the gate voltage as function of gate voltage due to local dielectric constant variability of the gate oxide for a FinFET structure computed with the IFM dielectric constant variability (blue curves) and modeling of the same effect as geometric thickness variability of the gate oxide layer (black curves). The dotted lines show results from statistical IFM and the dashed line for noise-like IFM.

### IFM for Gate Line-Edge Roughness Variability

IFM is suitable for the investigation of gate line-edge roughness (LER) variability. The effects of the self-aligned source and drain implant (for which the gate stack acts as the effective mask) is mimicked by applying correlated shifts to the side gates and the doping profiles. IFM supports such correlation of two or more variability sources through the random field approach: An abstract dimensionless field of random scaling factors is defined throughout the device and used to scale the local amplitudes for the respective variability models.

Note that the meshing requirements around the gate edges for IFM LER simulations are a bit different compared to regular TCAD simulations. In particular, it is necessary to adequately resolve the side gate interfaces. It is therefore recommended to first compare IFM results and regular TCAD simulations for structures with a uniformly changed gate length and then rerun the IFM simulations for the desired finite correlation length.

### Enhancement to the Noise-like Impedance Field Method

The noise-like impedance field method was enhanced to now also allow to geometrically restrict the variability source to a box-shaped region. Also users can now separate the random doping variability from donors and acceptors. Such capabilities were already available for the statistical impedance field method.

### Mobility Enhancements

#### Inversion and Accumulation Layer Mobility Model Enhancements

The Inversion and Accumulation Layer Mobility Model (IALMob) is often used when simulating nanometer scale devices such as FinFETs. For the 2014.09 J-release, the following enhancements have been made to IALMob:

- ▶ The model now includes explicit dependencies on layer thickness. These dependencies enter the model in two places:
  - IALMob uses a weighting function to transition between 2D Coulomb scattering (where there is strong quantization) and 3D Coulomb scattering (where there is weak quantization). Previously, the primary dependency of the weighting function was normal electric field. In this release, the weighting function has been modified to include a dependency on layer thickness. For small layer thickness, the weighting function will favor 2D Coulomb scattering regardless of normal electric field.
  - A dependency on layer thickness is also included in a prefactor for 2D Coulomb mobility. For large layer thickness, 2D Coulomb mobility is unaffected. For small layer thickness the prefactor results in an increase in 2D Coulomb mobility.
- ▶ New parameters have been introduced that make it possible to calibrate 2D phonon scattering and surface roughness scattering separately in "inversion" and "accumulation" regions.

#### Mole-fraction Dependency for the ThinLayer Mobility Model

Parameters used in the ThinLayer model can now include a dependency on mole-fraction. This allows the model to be calibrated for composition-dependent materials such as silicon germanium.

#### New RCS and RPS Mobility Degradation Models

The RCS and RPS components of the `Lombardi_highk` mobility model are now available as separate mobility degradation models named RCS and RPS, respectively. There are several reasons why these new models should be used instead of their `Lombardi_highk` counterparts:

- ▶ Specifying RCS and/or RPS in a Sentaurus Device command file makes it more clear what degradation component is being included in the simulation.



- ▶ The RCS and RPS models are much more efficient than the corresponding components of `Lombardi_highk` (simulations will be faster).
- ▶ The RCS and RPS models support the ability to specify stress factors for individual mobility components. `Lombardi_highk` does not support this feature.

### Mobility Stress Factor PMI

Sentaurus Device now supports a Mobility Stress Factor physical model interface (PMI) that will enable users to create PMI models that calculate isotropic stress-dependent enhancement factors for mobility. In addition to dependencies on constant fields, such as the stress tensor and mole-fraction, this type of PMI also allows a dependency on normal electric field to be included in the calculation.

### Anisotropic Scharfetter-Gummel Approximation

A novel discretization scheme for anisotropic transport equations is introduced in this release. The AnisoSG scheme supports simulations with the following anisotropic model parameters:

- ▶ Poisson equation: anisotropic dielectric permittivity  $\epsilon$ .
- ▶ Heat equation: anisotropic thermal conductivity  $\kappa$ .
- ▶ Current continuity equation: anisotropic mobility  $\mu$ .

The `AnisoSG` addresses shortcomings in the two previous discretization schemes (`AverageAniso` and `TensorGridAniso`). In both previous schemes, the accuracy of the solution depends on the relative orientation of the anisotropic direction and the mesh element edges. In particular the `AverageAniso` scheme uses a local linear transformation, which transforms an anisotropic problem to an isotropic case. This method has good accuracy only if the transform mesh is a Delaunay mesh.

Unfortunately it is quite impractical for a user to ensure that this condition is met.

The `TensorGridAniso` discretization scheme gives correct results if the anisotropy direction and direction of the mesh edges are closely aligned. This condition is often met for devices with planar geometry and can easily be verified. This discretization scheme is the most robust one and the fastest, and can be the method of choice if the aforementioned conditions are met. However, for arbitrary mesh orientations the accuracy of this discretization scheme may be reduced.

The new `AnisoSG` discretization scheme is a nonlinear multipoint modification of the well-known Scharfetter-Gummel approximation and guarantees accurate results for any mesh orientation independent of the anisotropy orientation. As result the new discretization scheme is the most accurate choice for strongly anisotropic transport problems for any Delaunay mesh. Due to the somewhat larger computational effort a small runtime penalty may be observed when using this discretization scheme.

As an illustration, Figure 24 shows the  $I_c V_c$  characteristics for a 3D 4H-SiC nIGBT. If the anisotropy direction is set to the (1 1 1) axis the  $I_c V_c$  results obtained with the `TensorGridAniso` discretization scheme deviate somewhat from the correct solution from the `AnisoSG` discretization scheme.

If the anisotropy direction is set to the (100) axis the  $I_c V_c$  results obtained with the `AnisoSG` and the `TensorGridAniso` discretization scheme are virtually identical (not shown), because here indeed physical current predominantly flows parallel to mesh edges and the anisotropy direction is also aligned with the mesh.

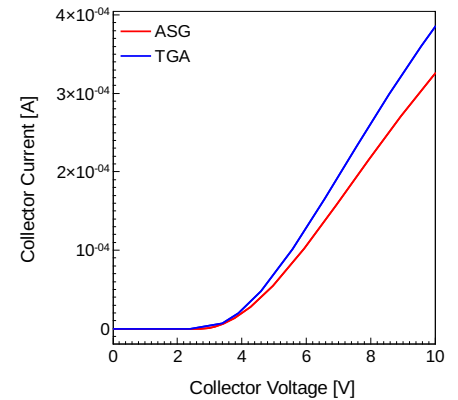
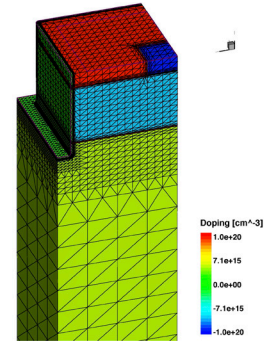


Figure 24:  $I_c V_c$  characteristics for a 3D 4H-SiC nIGBT (shown on the left) for an anisotropy direction on (111). Red curve: results based on the new `AnisoSG` discretization scheme. Blue curve: corresponding results using the `TensorGridAniso` discretization scheme.

### Miscellaneous Enhancements

#### Stress-Dependent Avalanche Generation

Experimental evidence has shown that impact ionization efficiency increases with strain and that the strain dependence of impact ionization efficiency is primarily due to the narrowing of the energy bandgap caused by strain [9]. This suggests that a simple way to include a dependency on stress in the avalanche generation models available in Sentaurus Device is by introducing a dependency on bandgap energy.

For the J-2014.09 release, the avalanche generation models available in Sentaurus Device (with the exception of the Hatakeyama

model) have been enhanced to include an optional dependency on bandgap energy. When this option is utilized, changes to the bandgap caused by stress, and also changes caused by bandgap narrowing, will have a direct impact on the calculated impact ionization generation rates inside the device.

### *Parallelized nonlocal barrier tunneling*

The simulation of nonlocal tunneling at interfaces, contacts, and junctions is computationally intensive. With the newly parallelized algorithm, computations involving nonlocal tunneling run faster in the multithreading mode.

### **Advanced Calibration for Device Simulation**

Advanced Calibration for Device Simulation Version J-2014.09 provides new features and enhancements for InGaAs, Silicon, and SiliconGermanium based devices as well as for WBG devices formed on SiliconCarbide or III-V Nitrides.

For SiliconCarbide updated parameter files for 4H-SiC and 6H-SiC are available in the MaterialDB folder of Sentaurus Device. The new parameter files contain calibrated temperature-dependent impact ionization coefficients and incomplete ionization parameters for Phosphorus.

For InAs, GaAs, and InGaAs, parameter files containing calibrated quantization parameters for the Density Gradient and the MLDA/MultiValley models for bulk, thin film, and FinFET devices are delivered. Furthermore calibrated model parameters for band gap narrowing and bulk mobility are now available for III-V Arsenides. All models are fully mole fraction dependent and tested on planar and FinFET devices.

Parameters for the contact resistance between PtSi and NiSi are extracted and presented in the AdvancedCalibration Device manual for the `schottkyresist` model for Silicon. New parameter sections for the `RCSMobility` and `RPSMobility` models that will replace the `Lombardi_`

`highk` model in Sentaurus Device and for the `MultiValley` model are introduced into the parameter files for Silicon and SiliconGermanium.

### **Electrical and Thermal Distributed Resistance Model Enhancements**

Electrical and/or thermal boundary resistances at interfaces can be emulated by inserting a thin material layer with a specific resistivity between the two materials, but this approach is practical only for relatively flat interfaces. The distributed electrical and thermal resistance models remove this limitation by allowing the user to directly specify the electrical and/or thermal resistances interface-wise in the Sentaurus Device command file.

The electrical distributed resistance model has also been made available for semiconductor/semiconductor and metal/metal interfaces besides the semiconductor/metal interfaces already available in the previous releases. In addition, for consistency, for the metal/semiconductor interfaces the model has been re-implemented using double-point approach used for semiconductor/semiconductor and metal/metal interfaces. The model is now available at all electrical conductive interfaces and contacts.

The thermal distributed resistance model has also been extended to metal/metal and metal/insulator interfaces besides the semiconductor/semiconductor interfaces already available in the previous releases. The model is now available at all interfaces.

### **Schottky Resistance Model Enhancements**

A new Schottky resistance PMI has been introduced to allow more flexibility in modeling Schottky resistance at contacts and metal/semiconductor interfaces. The new PMI allows the user to define the Schottky resistance as an arbitrary function of lattice temperature, carrier temperatures, electron affinity, bandgap, bandgap

narrowing, conduction and valence band effective density of states and effective intrinsic density.

Additionally, a general new PMI run-time function has been introduced to allow access from a PMI to any mole-dependent and constant model parameter visible across Sentaurus Device. In particular, in the context where the PMI does not have support for mole-fraction parameters, the new function allows the Schottky resistance PMI to use the built-in Schottky resistance mole-fraction dependent parameters.

### **Tcl Current Plot**

The current plot section offers a convenient mechanism to include additional data to the current plot file. It is possible to monitor quantities at a specific location, or to compute averages or integrals over specified domains such as regions, materials, wells, or windows. Until this release it was only possible to add standard Sentaurus Device quantities to the current plot file without resorting to the current plot PMI (physical model interface) or post-processing in Sentaurus Visual.

### **Current Plot Tcl Formula**

Starting with the J-2014.09 release it is now possible to use the Tcl interpreter to evaluate formulas and add the results to the current plot file. As an example let us consider the electron conductivity  $\sigma_n$  given by

$$\sigma_n = qn\mu_n \quad \left[ \frac{1}{\Omega\text{cm}} \right]$$

Here  $n$  denotes the electron density, and  $\mu_n$  denotes the electron mobility. The following specification in the Sentaurus Device command file adds the average electron mobility in the channel region to the current plot file:

```
CurrentPlot {
  Tcl (
    Formula = "set q 1.602e-19
set n [tcl_cp_ReadScalar
eDensity]
set mu [tcl_cp_ReadScalar
eMobility]
```



```

        set value [expr $q *
$ln * $mu]"
    Dataset = "Channel
eConductivity"
    Function = "Conductivity"
    Operation = "Average Region
= Channel"
)
}

```

The Tcl statements in Formula are evaluated on each mesh vertex. Sentaurus Device provides a `tcl_cp_ReadScalar` function to access the various fields on the local vertex. The standard Tcl `expr` function can then be used to evaluate the arithmetic expression for the electron conductivity  $\sigma_n$ .

The `Operation` parameter specifies the desired operation, in this case the averaging over the channel region. All the familiar operations from the standard current plot section are available, such as `average/minimum/maximum/integral over domains` such as `regions/materials/wells/windows`.

The `Dataset` and `Function` parameters determine the header information in the current plot file.

### Current Plot Tcl Interface

While Tcl formulas cover most applications, there are always cases that require additional support, for example:

- ▶ Calculation of integrals or averages over non-standard domains, such as user-defined cuts or interfaces
- ▶ Non-local effects such as tunneling
- ▶ Evaluation of quantities that depend on geometrical features, such as the distance to surfaces or interfaces

For such cases Sentaurus Device also provides a Tcl alternative to the current plot PMI. In the command file this alternative is selected by specifying the Tcl source code within the Tcl statement:

```

CurrentPlot {
    Tcl {Tcl = "source
conductivity.tcl"}
}

```

In this example the actual Tcl source code is stored in a separate file `conductivity.tcl` for convenience.

Similar to the C++ PMI the current plot Tcl interface relies on a comprehensive set of run-time support functions to access the entire device mesh and the data fields defined on the mesh. A user may prefer to use the Tcl interface as opposed to the older PMI interface for a variety of reasons:

- ▶ The interface does not require any C++ knowledge and access to a C++ compiler.
- ▶ The usability is improved since no separate preprocessing step is required in Sentaurus Workbench to compile the PMI source code.
- ▶ The new option enables quick prototyping within the familiar Tcl language.

### Mechanical Stress Solver

Mechanical stress has become a major effect in modern semiconductor devices. It is no longer sufficient to consider constant stress tensors only, but the stress in a device may actually change during its operation:

- ▶ Different materials have different thermal expansion coefficients. This thermal mismatch leads to stress changes as a function of the lattice temperature of the device. The influence of thermo-mechanical stress on device performance is investigated in [10] and [11].
- ▶ The electrical degradation of GaN HEMT's is sometimes attributed to the inverse piezoelectric effect, see [12].
- ▶ Gate-dependent polarization charges in GaN HEMT's are reported in [13].
- ▶ Piezoresistive and piezoelectric materials are the key components of piezoelectronic transistors, see [14].

A first version of the mechanics solver in Sentaurus Device has been introduced in the I-2013.12 release. With the mechanical stress solver, thermal mismatch stress between different materials can be analyzed. In the I-2013.12 release, only a simplified approach based on the global device temperature was

available. Starting with the current J-2014.09 release, local lattice temperature distributions can be taken into account.

### AC analysis in single-device mode

Many applications study stationary and transient behavior of single devices. However, performing a small signal (AC) analysis in S-Device for the same device requires not only an ACCoupled solve statement but also the specification of a suitable System section, defining the system nodes contained in the admittance matrices computed by the AC analysis.

With the new J-2014.09 release, a suitable AC system is now internally constructed if requested by the single keyword `ImplicitACSystem`. This makes transitions from DC or transient simulations of single devices to corresponding AC analysis command files much easier. In fact, each voltage controlled electrode is automatically connected to a system node, which in turn is connected to a suitable voltage source reflecting the DC and transient boundary conditions at the contact. Goal statements in `quasistationary` ramps formulated for the contact are automatically translated into ramps of corresponding parameters of the connected voltage source. Additionally, Sentaurus Device generates a suitable AC extraction file which contains both DC and AC response variables automatically for the relevant system nodes. The implicit AC system is essentially completely invisible for the user.

### III-V Band and Mobility Modeling

Accurate modeling of the performance of devices with III-V materials requires the treatment of their more complicated band structure. In particular, for low band gap semiconductors, the band nonparabolicity plays an important role in device behavior. Also, for thin layer devices, it is important to account for geometrical quantization which produces a dependence of the carrier transport on the layer thickness.



Geometrical quantization is usually strong in III-V materials because of the small electron effective mass in the  $\Gamma$  valley. Such quantization creates a band gap widening effect which can be clearly seen in the capacitance-voltage (CV) curves shown in Figure 25 for 5, 7.5 and 15 nm single-gate InGaAs structures. To perform such CV simulations with Sentaurus Device the multi-valley MLDA quantization model was developed further to account for band nonparabolicity and carrier confinement between two interfaces. This figure compares the multi-valley MLDA results with Schrödinger-Poisson and shows good agreement between the two modeling approaches.

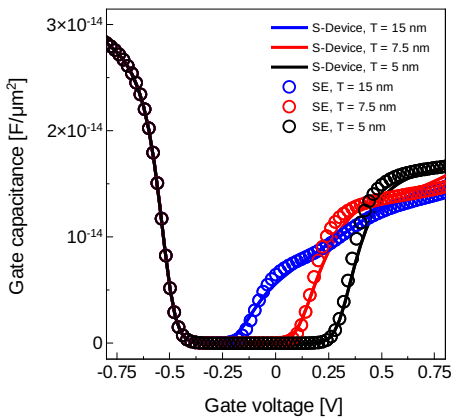


**Figure 25:** The gate capacitance of single-gate  $\text{In}_{0.53}\text{Ga}_{0.47}\text{As}$  structures computed with multi-valley MLDA model (lines) and Schrödinger-Poisson in S-Band (symbols) for 5, 7.5 and 15 nm layer thicknesses.

In addition to the bandgap widening effect there is also a change of the carrier transport properties in thin III-V layers. The multi-valley Subband mobility correction models were extended to work with arbitrary bands of III-V materials. Together with the multi-valley MLDA model extensions, this makes it possible to account for the effect of geometrical confinement in the carrier transport masses, scattering rates, and correspondingly in the mobility. Figure 26 shows the electron mobility versus the layer thickness in a InGaAs device where the results of the Subband model are shown to agree well to the literature and experimental data.

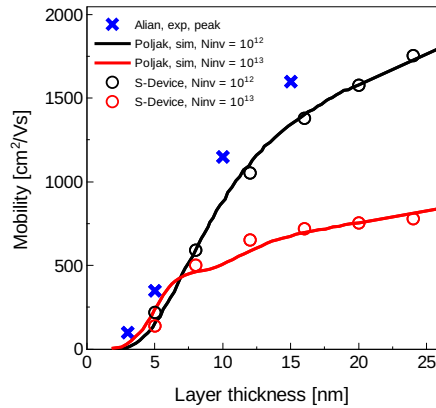


**Figure 26:** Total mobility versus the layer thickness for  $N_{inv} = 10^{12} \text{ cm}^{-2}$  and  $10^{13} \text{ cm}^{-2}$  in single-gate  $\text{In}_{0.53}\text{Ga}_{0.47}\text{As}$  structure.

The stress effect in the mobility is simulated with the linear deformation potential model applied for each valley and a stress-related Gamma valley effective mass change. Figure 27 shows Sentaurus Device simulation and literature data for the strain-induced change of the conduction band effective mass and momentum relaxation in InGaAs. These results predict that for 0.5% biaxial strain the mobility change is about just 10%.

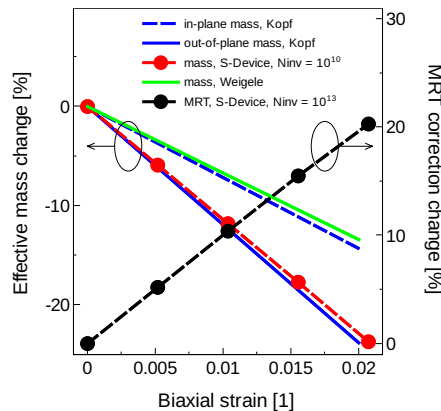


**Figure 27:** Strain-induced change of the conduction band effective mass and MRT correction in a 24 nm  $\text{In}_{0.53}\text{Ga}_{0.47}\text{As}$  double-gate structure, and comparison of the mass change to literature data.

## Sentaurus Device Opto and EMW Enhancements

Several optical enhancements have been introduced in Sentaurus Device. The unified optical generation interface adds a new excitation that allows the user to superimpose a modified Gaussian shape onto different shape functions of illumination, effectively creating a spatial Gaussian beam type of excitation. In EMW, new features have been implemented to improve its utilization in CMOS image sensor, detector and solar cell designs. EMW can import spatially varying carrier densities, temperature, etc., to create an inhomogeneous CRI profile, thereby facilitating the device simulation results to be fed back to the optical (EMW) simulation. Recent interest in broadband simulations has prompted various improvements in EMW's broadband capabilities. Oversampling can be controlled to ensure accelerated DFT (Discrete Fourier Transform) extraction of broadband results without losing signal information. The most important part for an accurate broadband EMW (FDTD) simulation is fitting accurate poles for the various dispersive models. This is discussed in more detail in the next few paragraphs.

The dispersive nature of light propagating through an absorbing material is typically characterized by a frequency-dependent CRI. During optical (EMW) simulations, this CRI is directly specified via a wavelength-dependent table of  $n$  (index of refraction) and  $k$  (extinction coefficient) values defined inside the material parameter file. Although the CRI table can be applied directly on a per wavelength basis in EMW simulations, it is good practice to first fit the CRI table of values to an appropriate dispersive media model prior to running simulations. To highlight this point, a few circumstances where this approach should be applied are discussed as follows.

At wavelengths where a material is highly absorptive ( $k > n$ ), the default settings in EMW will compute a negative value for the real part of the permittivity ( $\text{Re}[\epsilon] = n^2 - k^2$ ). If left unresolved, this can quickly lead to numerical instability. To avoid this problem, EMW detects this problem and automatically applies a large value of conductivity to the material which forces it to act like a perfect electric conductor (PEC). However, this auto-correction results in a change in the material properties and effectively masks the dispersive nature of the material defined by the CRI table.

On the other hand, when broadband EMW simulation is used with defined CRI tables for each material, the single values of  $n$  &  $k$  defined for the central wavelength of the broadband pulse are applied throughout the entire simulation. The result is that the dispersive nature of the material over the simulated spectral range is not properly accounted for.

To avoid these problems, it is recommended that prior to running an EMW simulation, the user performs a curve-fitting of the CRI data to one (or a combination) of the available dispersive media models in EMW. A proper fitting ensures stability and can improve the overall accuracy of EMW-computed optical absorption at both individual wavelengths and over a specific range of wavelengths.

This feature is implemented in the J-2014.09 release as a new library in Sentaurus Visual. The sequence for the fitting procedure is illustrated in Figure 28.

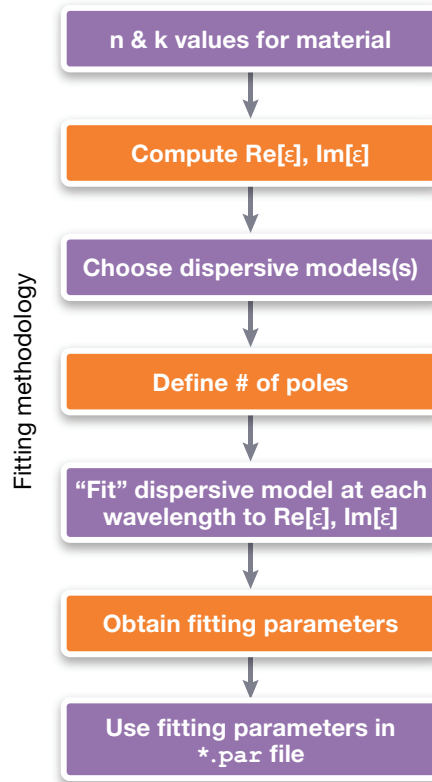


Figure 28: Fitting methodology for dispersive media.

The procedure begins with reading the  $n$  &  $k$  values from the CRI table in the material parameter file. Next, these values are used to compute the corresponding real and imaginary parts of the electric permittivity at each wavelength. The values of permittivity are then used in combination with a specific number of user-defined poles to fit the real and imaginary parts of the permittivity to a specific dispersive media model at each wavelength in the specified spectral range. The final result is a set of fitting parameters which are written into the dispersive model section of a new material parameter file which is automatically saved and available to the user. During subsequent EMW simulations, these fitting parameters help to ensure that EMW will not encounter numerical instabilities as discussed previously.

The new Sentaurus Visual `emw::fit` library in J-2014.09 release is a Tcl-based module that is loaded and used within a Sentaurus Visual script. This library provides the user with a way to specify all necessary parameters and settings to fit a material's CRI table to a specific dispersive media model. Using this script to drive Sentaurus Visual tool instance in Sentaurus Workbench allows the user to quickly build a streamlined workflow for fitting any number of materials as illustrated in Figure 29.

	1	2
Material	Silicon	Aluminum
dispersive_model	ModLorentz	DrudeModLorentz
npoles_a	2	1
npoles_b	0	5
wavel_MIN	300	300
wavel_MAX	1000	1000
epsinf_min	1	1
epsinf	1	1
epsinf_max	1.2	1.2
amp_min	1e-3	1e-3
amp	2	2
amp_max	10	10
freq_min	1e-3	1e-3
freq	9e14	1e13
freq_max	2e15	1e16
df1_min	1e-3	1e-3
df1	5e14	1e14
df1_max	1e15	1e17
df2_min	1e-3	1e-3
df2	2e15	1e14
df2_max	1e16	1e17
CRI_Tablestep	1	1
Maxiter	10	100

Figure 29: Workflow of Sentaurus WorkBench Project.

The library also provides a direct graphical user interface (GUI) with Sentaurus Visual allowing users to (1) modify all fitting parameters, (2) run material fittings, and (3) plot and visualize all results from directly within the Sentaurus Visual GUI using the Tcl Command window. During runtime, the `emw::fit` library reads in all user-supplied parameters in the Sentaurus Visual script (and/or parameterized Sentaurus Workbench variables) and performs a best fit of the material's CRI table to the desired dispersive media model. When the fitting is complete, the results are automatically plotted (or updated) in the Sentaurus Visual plotting window as shown in Figure 30. Additionally,



the `emw::fit` library also stores the current state of all fitting parameters which can be dynamically modified directly from within the Sentaurus Visual GUI TCL Command window to accommodate “on-the-fly” changes needed to adjust the accuracy and/or quality of the curve fitting to the available CRI data, as shown in Figure 31.

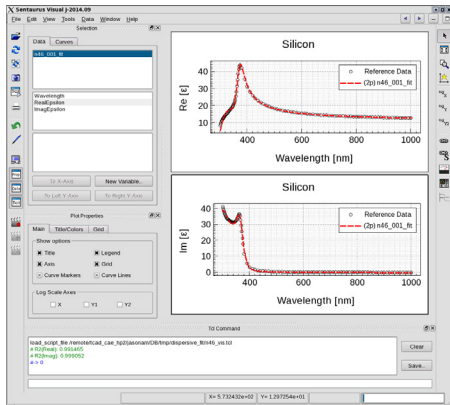


Figure 30: Silicon fit with 2-pole Modified Lorentz model.

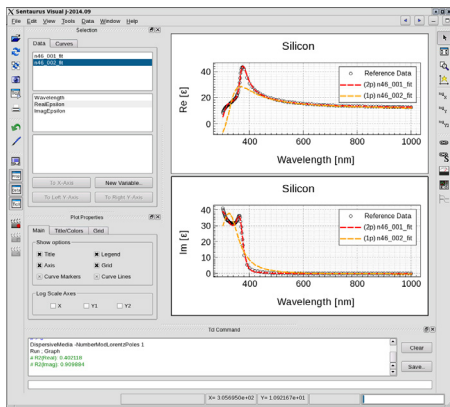


Figure 31: Updated Silicon fitting with 1-pole Modified Lorentz model.

## Sentaurus Device Monte Carlo New Channel Materials

In order to further enhance CMOS performance or to adjust the threshold voltage, silicon has already been replaced by silicon germanium (SiGe) as channel material in p-type devices. SiGe is now also being considered for n-type FinFETs. In release J-2014.09, electrons in Si<sub>1-x</sub>Ge<sub>x</sub> can be simulated for arbitrary molefraction x and

under arbitrary stress, thus generalizing the already existing capability for holes to n-type devices. Up to a molefraction of 85%, the electron band structure is considered to be Si-like, i.e. only  $\Delta$  valleys are taken into account. For higher Ge-content, a Ge-like band structure is adopted which also includes  $\Gamma$ - and L-valleys. Either an empirical pseudopotential band structure table or an accurate analytic two-band model can be used. The scattering mechanisms comprise Si-like and Ge-like phonon scattering and alloy scattering where the default value for the alloy scattering potential is adjusted to dedicated mobility measurements. This enables users to extend efficient stress- and orientation-engineering of nanoscale Si-FinFETs [14] to arbitrary n- and p-type SiGe FinFETs, including pure Ge-FinFETs [15].

For even further performance enhancement at low supply voltage, indium gallium arsenide (InGaAs) is being investigated for n-type devices. The III-V alloy can be simulated for electrons in release J-2014.09 based on pseudopotential band structure tables and including polar-optical phonon scattering and alloy scattering. This III-V simulation capability development is embedded in the project “Technology CAD for III-V Semiconductor-based MOSFETs (III-V MOS)” within the 7<sup>th</sup> Framework Program of the European Union.

## Improved Quantum Correction

In nanoscale multi-gate devices several effects need to be captured at the same time. In particular, the orientation-dependence of the effective mobility, as for example occurring in FinFETs with different crystallographic sidewall orientations [16], has to be reproduced without orientation-dependent calibration; otherwise, nanowires, for example, cannot be simulated since infinite many orientations around the transport direction are present. On the other hand, quantum-induced threshold voltage shifts and channel charge modulation have to be taken into account as well. One approach which allows these two

requirements to be fulfilled at the same time with high accuracy is surface roughness scattering based on a combination of 15 % diffusive and 85 % specular scattering (see the discussion in [14]) together with a quantum correction using an effective oxide permittivity and an effective work function extracted from a previous quantum drift-diffusion simulation. It has turned out that this quantum correction involves inaccuracies for non-planar multi-gate devices. This issue can be solved by using a second effective work function in the on-state, the value of which is ramped together with the gate voltage above the threshold voltage. The three quantum parameters (effective oxide permittivity and two work functions in subthreshold and on-state) can be efficiently computed from a 2D cross-section of the device and were shown to accurately reproduce quantum drift-diffusion simulations also in the short-channel regime [17]. This procedure is performed automatically in a TCAD workbench project without any user interaction and enables also the efficient use of 2D Schrödinger-Poisson solutions replacing density-gradient as a quantum reference [15].

## Subband and Inversion-Layer Mobility Calculator

Several enhancements have been made to the calculation of low-field mobility in Sentaurus Band Structure, including the addition of a new screening model, the addition of polar optical phonon scattering for the treatment of III-V materials and the first implementation of mobility calculations for 2D FinFET and nanowire cross-sections.

## Lindhard TDF Screening

The tensorial form of the Lindhard screening model has been generalized so that it can now be used by any scattering model, including Coulomb, surface roughness, alloy, and the new polar optical phonon scattering model. This screening model can be selected using `screening=LindhardTDF` on the corresponding `Physics` command. This tensorial model is the most accurate



screening model available in the program and is the appropriate model to use for double-gate geometries.

### III-V Mobility Calculations

In this release, polar optical phonon (POP) scattering has been added to the list of available scattering mechanisms for mobility calculations in 1D structures. POP scattering is typically the dominant phonon scattering mechanism in III-V materials. POP scattering is implemented as an anisotropic scattering mechanism within the Kubo-Greenwood formalism and can be screened using the new Lindhard TDF model.

Figure 32 shows a calculation of the low-field electron mobility in a bulk  $\text{In}_{0.53}\text{Ga}_{0.47}\text{As}$  nMOSFET using the new POP scattering model along with Coulomb, non-polar phonon, alloy, and surface roughness scattering. After calibration of the interface charge and surface roughness parameters, good agreement with measurement is obtained. Also shown are the contributions of the different scattering mechanism. In this device, Coulomb and surface roughness scattering dominate the mobility with moderate contributions from screened alloy and POP scattering.

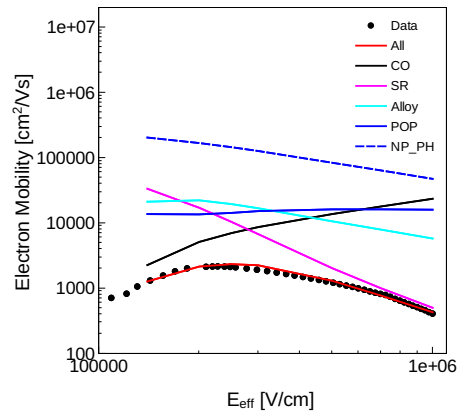


Figure 32:  $\text{In}_{0.53}\text{Ga}_{0.47}\text{As}$  nMOSFET mobility computed using the new III-V mobility capability in Sentaurus Band Structure compared to measurement data [11]. The contributions from different scattering mechanisms are shown.

### Mobility Calculations for 2D Structures

The Kubo-Greenwood formalism has been extended to enable the calculation of low-field mobility in 2D structures such as FinFET and nanowire cross-sections based on the subbands computed from the 2D Schrödinger solver. Either the parabolic or 6-band k-p Schrödinger solver can be used. In this first release of this capability, mobility calculations are limited to non-polar phonon scattering mechanisms. However, arbitrary strain and orientation conditions can be specified.

As an example, Figure 33 compares the diameter dependence of the phonon-limited hole mobility in a Si pMOS circular nanowire for two different channel orientations. For this example, the 2D 6-band k-p Schrödinger solver is used. The  $\langle 110 \rangle$  channel shows a striking increase in mobility as the diameter is decreased due to an advantageous decrease in the effective transport mass under increasing quantum confinement. The  $\langle 100 \rangle$  channel displays the opposite trend with diameter because the transport mass increases slightly with decreasing diameter and the mobility dependence becomes dominated instead by the increase in the phonon scattering rate at small diameters.

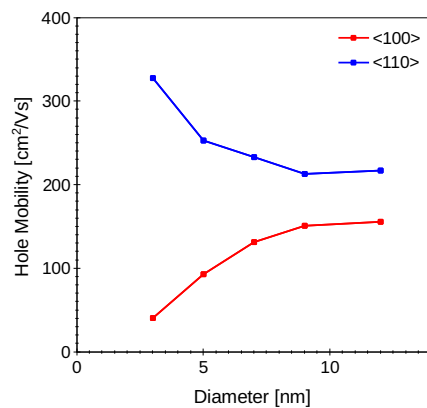


Figure 33: Diameter dependence of the phonon-limited mobility in a circular pMOS Si nanowire computed using the new 2D mobility calculation feature in Sentaurus Band Structure.  $\langle 110 \rangle$  and  $\langle 100 \rangle$  channels show opposite behavior. Mobility is computed at a fixed inversion charge per gated area of  $5 \times 10^{12} \text{ cm}^{-3}$ .

## Sentaurus Workbench

### 3-level Preferences

Sentaurus Workbench release J-2014.09 introduces global and site preferences in addition to the user preferences available in earlier versions. User preferences override global and site preferences. Site preferences override global preferences.

Initially user, site and global preferences are equivalent and contain release-specific Synopsys defaults. TCAD users typically configure Sentaurus Workbench preferences at the user level. Systems and TCAD administrators can change preferences at the global level and propagate required settings to the users by forbidding the corresponding user settings to take effect. When a company has multiple TCAD user groups distributed across different corporate sites, it may be useful to customize global preferences for all users at a specific site in the site preferences.

Global and site preferences are normally read-only for the regular TCAD users. All the preferences (global, site, user) can be viewed and configured in the SWB Preferences dialog box. The user can configure global and site preferences only if the write access to the corresponding files is available, otherwise global and site preferences are accessible in a view-only mode.

When Sentaurus Workbench release J-2014.09 is launched for the first time, it can pick up preferences from the latest previous TCAD release and convert old preferences to the new ones. This conversion is applied separately on the global, site, and user levels. Conversion does not trigger saving the preference file automatically. To store the preference file, open the SWB Preferences dialog box, check the consistency of the picked up settings and click Save or Apply.

## Auto-allocation of CPUs for Multi-Thread Jobs

Sentaurus Workbench release J-2014.09 can automatically detect the number of required CPU slots for multi-threaded simulation job and communicate it to the job cluster during submission. Sentaurus Workbench follows these steps for each node launched on a cluster:

1. Preprocess the node (if needed).
2. Inspect the node command file and identify parallelization-specific keywords that may depend on the tool syntax.
3. Check the command-line arguments in the tool properties (some tools support command-line options specifying the number of CPUs for parallelization).
4. Inspect the input TDR files (some tools store parallelization keywords there).
5. Consider the highest of all found numbers as the required number of threads.
6. Submit the job for execution on a chosen scheduling queue of the cluster. The number of parallel slots (CPUs) to allocate is communicated to the cluster using the resource requirements part of the job submission command. Multiple CPUs are allocated on the same host.

Sentaurus Workbench supports auto-allocation of CPUs for the following tools (with their corresponding tool database names): Sentaurus Band Structure (sband), Sentaurus Device (sdevice), Sentaurus Device Electromagnetic Wave Solver (emw), Sentaurus Interconnect (sinterconnect), Sentaurus Mesh (snmesh), Sentaurus Process (sprocess), Sentaurus Topography 3D (sptopo3d).

By default, the auto-allocation of CPUs for parallel jobs is disabled. You can enable this capability for desired tools in the tool database.

## More flexible visualization of results in Sentaurus Visual

Sentaurus Workbench J-2014.09 allows users to configure how to visualize new files in Sentaurus Visual in the preferences. There are 3 options:

- ▶ **Last Used:** the last-used Sentaurus Visual instance is selected in the dialog box (the one used last time to visualize files). This is the default option
- ▶ **Last Created:** last-launched Sentaurus Visual instance (the latest one launched in the current Sentaurus Workbench instance)
- ▶ **New Instance:** new Sentaurus Visual instance (SWB will launch a new Sentaurus Visual instance)

Sentaurus Visual Visualization dialog box allows users to apply file filters to the list of all the files that can be visualized for selected nodes, thus reducing the list and displaying only the needed files. Each file filter specifies one or more file patterns separated by space, and only files matching at least one pattern of the selected file filter is displayed. Sentaurus Workbench offers four predefined file filters: All XY-Plot Files (\*.plt, \*.plx); All Boundary Files (\*.bnd.tdr); All Mesh Files (\*.msh.tdr); All TDR Files (\*.tdr). You can introduce your own file filters in the Sentaurus Visual Visualization dialog box. Sentaurus Workbench will store these file filter and display them in the visualization menu: **Sentaurus Visual → Select by Type...**

## Improved Recoverability and Troubleshooting

Sentaurus Workbench release J-2014.09 can recover running projects when the gsub scheduling process running a SWB project is unexpectedly lost. This may happen if the host where swb and gsub ran shuts

down, if the terminal from which Sentaurus Workbench started was closed, or if the gsub process is killed unexpectedly if Sentaurus Workbench was launched on the interactive terminal running on the cluster. Sentaurus Workbench release J-2014.09 is able to return the control on the running project.

If the terminal from which Sentaurus Workbench was launched is closed or crashes, it may lead to the unexpected termination of swb instance and the running projects launched in this swb instance. If closing the terminal is inevitable and the user experiences an unwanted termination of running projects, users can force swb and gsub to run in a kind of “daemon” mode with environment settings which disconnect swb and gsub processes from the parent terminal process. As a result, the running projects will be completed even if the terminal process crashes or is terminated.

Sentaurus Workbench release J-2014.09 also introduces a diagnostics tool swbdiag which helps users check whether the Sentaurus Workbench infrastructure can run properly on two given hosts. This new troubleshooting tool is able to detect responsible network issues and incorrect environment settings. Such issues do usually happened due to specific operating system configuration or network problems. Problems may appear on new machines, as well as on previously good working hosts after their upgrade to a new version of the operating system.

## Sentaurus Visual Deformation feature

The Deformation feature allows altering structures according to a certain vector field that works as a guide for the deformation.



Every point that defines a region of the structure will be moved in the direction and magnitude of the guide vector.

The magnitude of the guide vector can be multiplied by a certain factor intensifying or attenuating the magnitude of the deformation.

The result is a different deformed structure based in the initial dataset.

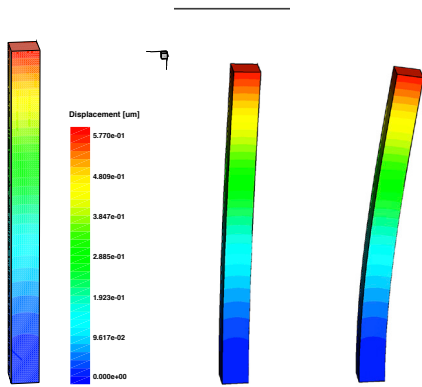


Figure 34: Deformation of structure. In the left the original structure, in the center deformed by a factor of 3 and in the right by a factor of 10.

### Min/Max location of a field

Now the minimum and maximum location of each field is stored and available for easily access and visualization.

Just by pressing a checkbox the user can activate markers in the plot that points to the location of the minimum or maximum values of a selected field.

Also a new functionality was added that allows searching for the location of the minimum or maximum values restrained to a specific set of restrictions. The restrictions can be the limitation of the spatial search space or available regions. It also allows the display of a field different from the one that is visualized.

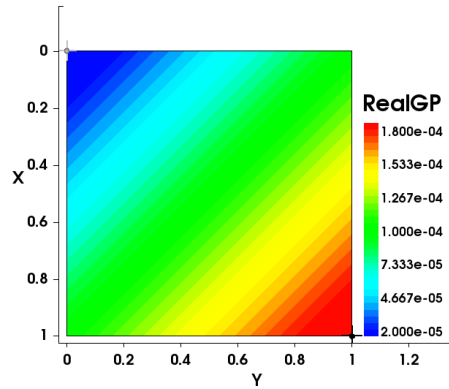


Figure 35: Minimum and maximum markers. The black marker is the maximum value and the white one the minimum.

### Axes ranges for TDR files

Sentaurus Visual has now the capability to set specific ranges on each axis of a 3D plot. Previously only XY and 2D plots had this capability.

When a range for an axis is set, this range is transformed into a vector with the same direction as the original axis. This vector is reflected into the vertical and horizontal vectors of the view screen where the maximum value is chosen and applied to the camera.

The result is a zoom into the plot that will represent in the best way the initial range that was set.

When the direction of the axis is perpendicular to the horizontal and vertical components of the camera, the projection will be 0. In this case the range can't be applied in the selected axis.

Modification of selected curves attributes for multiple curves

Sentaurus Visual now allows the edition of one curve property across multiple selected curves. Using the same "Curve Properties" dialog as before, the user can select multiple curves in the "selection panel" and apply properties at once to all the selected curves.

### Spherical rotation

The rotation of 3D plots using spherical angles to change the position and orientation of the camera is now available.

Sentaurus Visual uses theta, psi and alpha angles to rotate in spherical mode as shown in Figure 37

This type of rotation works in addition to the axis rotation already integrated in Sentaurus Visual.

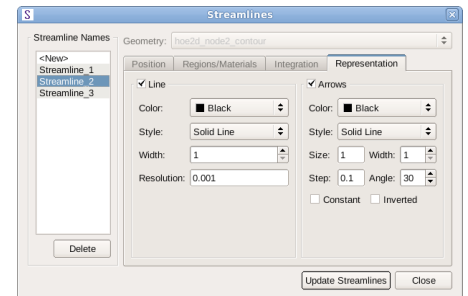
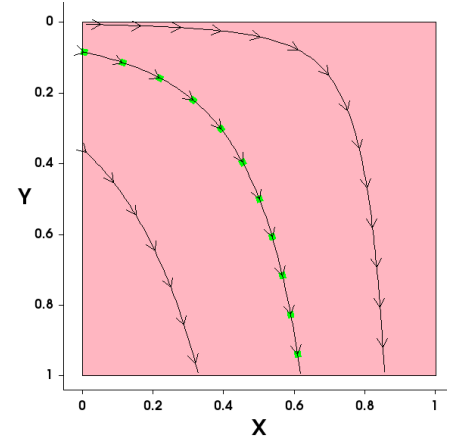


Figure 36: Streamlines Properties: at the bottom the "Streamlines dialog" and up the streamlines with the properties applied to them.



## Streamlines and Vectors properties

New improvements have been made in the vector area. These improvements are summarized in vector properties and streamlines properties (trace of a particle in vector field).

A new “Vector Field Properties” dialog and a new TCL command were added to Sentaurus Visual. With this command users can change the shape, color scaling and even separate the scaling of arrow heads and body for a vector representation. Sentaurus Visual Vector Properties Menu was also improved adding this new functionality to it.

Streamlines Dialog was modified and updated. Now the dialog also can highlight selected streamlines; this way helps the user to modify its properties. For this purpose a new command was created. This new command can modify the line properties, color, direction, etc, without recalculating the Streamline data, just its representation.

Also the streamlines creation was improved, now allows the user to create streamlines faster using multi-threading. The amount of desired threads can be set in Sentaurus Visual user preferences.

## Visualization of Mixed Mesh elements

Sentaurus Visual was improved of the visualization of various types of meshes in the same structure.

The types of meshes currently supported by Sentaurus Visual are: Triangles, Rectangles, Tetrahedrons, Pyramids, Prisms and Cuboids.

Also, field interpolation support was added for these structures. The field interpolation is done by calculating the barycentric coordinates of a specific point in relation of the cell containing the point and obtaining the interpolated value by a pondered sum between the values of each vertex and the barycentric coordinate attached to the vertex, i.e.,

$$\lambda = \lambda_e \cdot V_e$$

where  $\lambda$  is the barycentric coordinate of the point to be interpolated associated with the vertex  $e$  and  $V_e$  is the value of the field in the vertex  $e$ ;  $\lambda$  will be the interpolated value in the needed point.

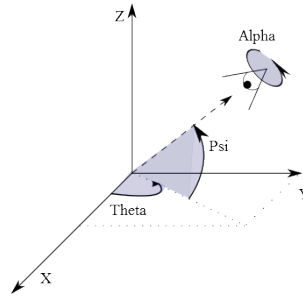


**Figure 37: Spherical rotation.** In the figure Theta, Psi and Alpha are shown in relation with the camera.

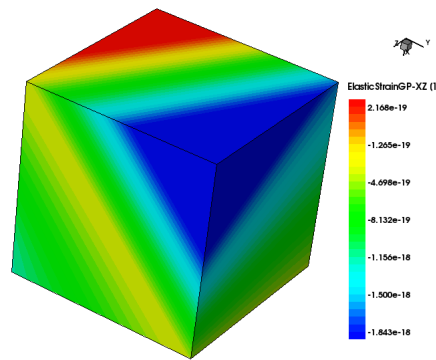


**Figure 38: Visualization of mixed mesh:** The figure shows a single cuboid with high order elements. The colors are the result of the interpolation of the data between its vertices.

## Interactive Interface to Sentaurus Process and Sentaurus Interconnect

The J-2014.09 release of Sentaurus Visual features an interface to Sentaurus Process and Sentaurus Interconnect for visualization of simulation results and control of the running simulation. A Simulation Control panel in Sentaurus Visual contains buttons to load a simulation command file and to control the simulation, an editor in which changes to the command file can be entered, as well as a window showing the

simulation log, see Figure 39. The following control buttons are available: Load, Save, Save As, Run, Pause, Run Step, and Reset. In addition, breakpoints can be inserted in the flow to pause the simulation execution at a particular step of the flow.

After starting the simulation using the control buttons, the structure and data is automatically updated while the simulation progresses. In 1D, the display shows an XY plot which tracks the evolving data fields, and when the simulation switches to 2D or 3D the display shows the structure with color mapped data fields. While the simulation is running, adjustments to the plot settings (axis ranges, field ranges, field selection, display of regions, display of mesh, etc) can be made via the standard Sentaurus Visual GUI menus and buttons. In addition, plot settings can be controlled from the Sentaurus Process or Sentaurus Interconnect input file using the graphics command which can be convenient when running and rerunning the same input file which is often required, for example, to create a new flow or for calibration-type activities. Newer plot settings override older settings whether they come from the Sentaurus Visual GUI or from the input file. Common plot setting arguments are: xmin, xmax, ymin, ymax, fields, field.1d.min, field.1d.max, field.min, field.max, display.all, display.border, display.bulk, display.field, display.mesh.

In 3D simulations, two plots are shown with the titles ‘bulk’ and ‘boundary’, see Figure 39. This is because in 3D simulations both representations are maintained separately by the simulation tools. Various simulation commands modify the structure only, the data only, or both the structure and data so that either the bulk, or in rare cases the boundary, is not always up to date. The plot with its title in bold shows the last updated information.

The current simulation step and other visual guidance is given in the editor part of the Simulation Control panel, see Figure 40. As the flow is being executed, a green triangle in the



left margin (in the same location as breakpoints) indicates the step that will be executed next. A red triangle indicates the step that is currently being executed. Already executed steps are indicated with a gray background. This part of the flow cannot be changed further. In addition, wherever the cursor is in the flow, its position is indicated by highlighting the line with a light yellow background.

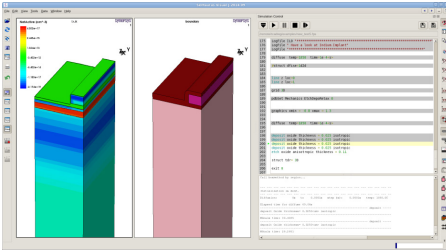


**Figure 39: Simulation control panel in S-Visual: At the top buttons to control the simulation execution, upper pane of Simulation Control panel shows command file loaded and lower pane shows simulation log output.**

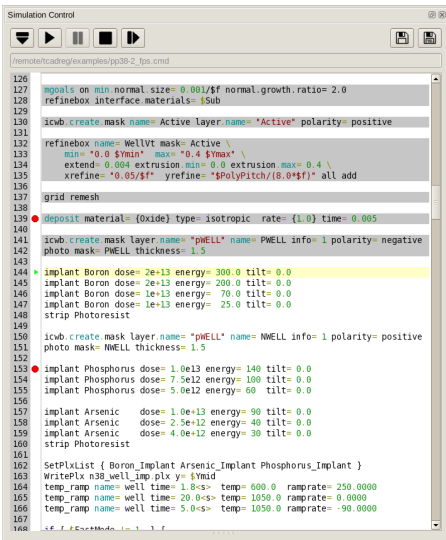


**Figure 40: Visual guidance in the editor including red dots as breakpoints, green triangle indicating step to be executed next, already executed steps with gray background, and cursor position on line with light yellow background.**

## New Applications Library

The TCAD Sentaurus release J-2014.09 is shipped with an expanded applications library, which now includes many of the application examples which previously were available on SolvNet only. This change acknowledges the fact not all TCAD users have easy access to the internet at their workplace. In order to accommodate the extra application examples the new application library contains only the input files to the simulation project.

To make it easy to find the application example several improvements are made:

- ▶ The application library uses folder names which clearly refer to a specific application area.
- ▶ All application examples are now named according to a consistent scheme: `<DeviceType>_<Technology>_<Material>_<SimulationType>_<Dimension>`
- ▶ (Some qualifiers may be omitted if they are not important for the specific application example.)
- ▶ The TCAD Sentaurus Tutorial now contains four interactive search pages, which can be accessed by clicking the looking glass icon on the front page of the Tutorial.
- ▶ The first search page lists all application examples by application area and provides links to the project directories and the project documentation.
- ▶ The second search page allows users to select one or more TCAD tool command or option and will show users all application examples which use these commands or options. This is a convenient way to quickly find a usage example for a given tool command.
- ▶ The third search page performs a full-text search of all application example documentations as well as the TCAD Sentaurus Tutorial.

- ▶ Lastly, the fourth search page performs a full-text search of all application example command files.

The new application library makes available to users a wealth of application examples along with a search tool to quickly find the right example.

Please note that you can still find additional application examples, which may have been created after the release date, on SolvNet and on the FTP servers

[https://solvnet.synopsys.com/redauthftp/caf/TCAD\\_Sentaurus\\_Applications\\_<release>](https://solvnet.synopsys.com/redauthftp/caf/TCAD_Sentaurus_Applications_<release>) where <release> is J-2014.09, H-2013.12, or G-2012.03.

## References:

- [1] R. Cerny, V. Chab, and P. Prikryl, "Numerical simulation of the formation of Ni silicides induced by pulsed lasers," Computational Materials Science, vol. 4, no. 3, pp. 269-281, 1995.
- [2] W. Hu, C.H. Wang and S. Barter, "Analysis of Cyclic Mean Stress Relaxation and Strain Ratcheting Behaviour of Aluminium 7050", Department of Defence, Defence Science and Technology Organization, DSTO-RR-0153, 1999.
- [3] P. Armstrong, C. Frederick, "A Mathematical Representation of the Multiaxial Baushinger Effect", Tech. Rep., Central Electricity Generating Board, Berkeley, UK, RD/B/N731, 1966.
- [4] M.P. Phaniraj, M.J.N.V. Prasad, A.H. Chokshi, "Grain-size distribution effects in plastic flow and failure," Material Science and Engineering: A, 463,1-2, pp. 231–237, 2007.
- [5] L. Mei and R. W. Dutton, "Process Simulation Model for Multilayer Structures Involving Polycrystalline Silicon" IEEE Transactions on Electron Devices, vol. ED-29, no. 11, pp. 1726-1734, 1982.
- [6] P. Chaudhari, "Grain Growth and Stress and Stress Relief in Thin Films", Journal of Vacuum Science and Technology, v. 9, pp.520-522 (1972)
- [7] W. D. Nix, "Mechanical Properties of Thin Films", Department of Materials Science and Engineering, Stanford University.



- [8] T. Iriasawa, et al., "On the Origin of Increase in Substrate Current and Impact Ionization Efficiency in Strained-Si n- and p-MOSFETs," *IEEE Trans. Electron Devices*, vol. 52, no. 5, pp. 993-998, May 2005.
- [9] Huang, G. Y., & Tan, C. M. (2011, June). Electrical-Thermal-Stress Coupled-Field Effect in SOI and Partial SOI Lateral Power Diode. *IEEE Transactions on Power Electronics*, 26(6), 1723-1732.
- [10] Tan, C. M., & Huang, G. (2011, October). Comparison of SOI and Partial-SOI LDMOSFETs Using Electrical-Thermal-Stress Coupled-Field Effect. *IEEE Transactions on Electron Devices*, 58(10), 3494-3500.
- [11] Jungwoo, J., & Del Alamo, J. (2006). Mechanisms for Electrical Degradation of GaN High-Electron Mobility Transistors. *IEDM*, (pp. 11-13).
- [12] Ashok, A., Vasileska, D., Goodnick, S. M., & Hartin, O. L. (2009, May). Importance of the Gate-Dependent Polarization Charge on the Operation of GaN HEMTs. *IEEE Transactions on Electron Devices*, 56(5), 998-1006.
- [13] Zhang, Y., Liu, Y., & Wang, Z. L. (2011, July 19). Fundamental Theory of Piezotronics. *Advanced Materials*, 23(27), 3004-3013.
- [14] F. M. Bufler, F. O Heinz, and L. Smith., "Efficient 3D Monte Carlo Simulation of Orientation and Stress Effects in FinFETs," *International Conference on Simulation of Semiconductor Processes and Devices (SISPAD)*, Glasgow, Scotland, pp. 172-175, September 2013.
- [15] F.M. Bufler, "Monte Carlo simulation of nanoelectronic devices," *QuantumHagen Workshop on Modeling of Electronic Devices and Materials at the Nanoscale*, Copenhagen, Denmark, July 2014 (<http://www.quantumwise.com/conference2014/abstracts.html#bufler>).
- [16] K. Akarvardar et al., "Impact of fin doping and gate stack on FinFET (110) and (100) electron and hole mobilities," *IEEE Electron Device Lett.*, vol. 33, pp. 351-353, 2012.
- [17] F.M. Bufler and L. Smith, "3D Monte Carlo Simulation of FinFET and FDSOI Devices with Accurate Quantum Correction," *J. Comput. Electron.*, vol. 12, pp. 651-657, 2013.
- [18] Xuan et al. "Submicrometer Inversion-Type Enhancement-Mode InGaAs MOSFET with Atomic-Layer-Deposited Al<sub>2</sub>O<sub>3</sub> as Gate Dielectric," *IEEE Electron Device Letters*, vol. 28, no. 11, 935 (2007).
- [19] Sentaurus Topography 3D User Guide, Version J-2014.09. Synopsys Inc., Mountain View, CA, USA.